February 8, 2008

Muon Capture on the Deuteron

The MuSun Experiment

MuSun Collaboration

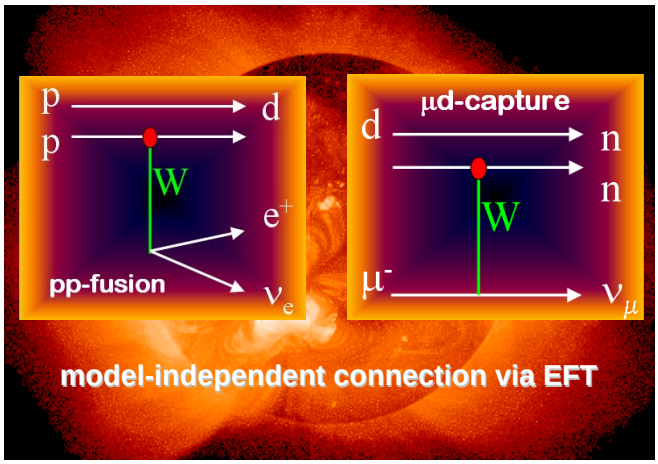

http://www.npl.uiuc.edu/exp/musun

V.A. Andreev[a], R.M. Carey[e], V.A. Ganzha[a], A. Gardestig[h], T. Gorringe[d], F.E. Gray[g], D.W. Hertzog[b], M. Hildebrandt[c], P. Kammel[b], B. Kiburg[b], S. Knaack[b], P.A. Kravtsov[a], A.G. Krivshich[a], K. Kubodera[h], B. Lauss[c], M. Levchenko[a], K.R. Lynch[e], E.M. Maev[a], O.E. Maev[a], F. Mulhauser[b], F. Myhrer[h], C. Petitjean[c], G.E. Petrov[a], R. Prieels[f], G.N. Schapkin[a], G.G. Semenchuk[a], M.A. Soroka[a], V. Tishchenko[d], A.A. Vasilyev[a], A.A. Vorobyov[a], M.E. Vznuzdaev[a], P. Winter[b]

[a]Petersburg Nuclear Physics Institute, Gatchina 188350, Russia
[b]University of Illinois at Urbana-Champaign, Urbana, IL 61801, USA
[c]Paul Scherrer Institute, CH-5232 Villigen PSI, Switzerland
[d]University of Kentucky, Lexington, KY 40506, USA
[e]Boston University, Boston, MA 02215, USA
[f]Université Catholique de Louvain, B-1348 Louvain-la-Neuve, Belgium
[g]Regis University, Denver, CO 80221, USA
[h]University of South Carolina, Columbia, SC 29208, USA

Co-spokespersons underlined.

Abstract: We propose to measure the rate Λ_d for muon capture on the deuteron to better than 1.5% precision. This process is the simplest weak interaction process on a nucleus that can both be calculated and measured to a high degree of precision. The measurement will provide a benchmark result, far more precise than any current experimental information on weak interaction processes in the two-nucleon system. Moreover, it can impact our understanding of fundamental reactions of astrophysical interest, like solar pp fusion and the $\nu + d$ reactions observed by the Sudbury Neutrino Observatory. Recent effective field theory calculations have demonstrated, that all these reactions are related by one axial two-body current term, parameterized by a single low-energy constant. Muon capture on the deuteron is a clean and accurate way to determine this constant. Once it is known, the above mentioned astrophysical, as well as other important two-nucleon reactions, will be determined in a model independent way at the same precision as the measured muon capture reaction.

At the moment the experimental situation on $\mu + d$ capture is inconclusive. An experiment with 10% errors agrees with theory, the most precise measurement with 6.2% uncertainty disagrees by three standard deviations from the best recent calculation, which has 1% uncertainty. If true, such a discrepancy would have major ramnifications on the above mentioned astrophysical processes. The required significant improvement in precision expected with the MuSun experiment became feasible by the advanced techniques developed for the MuCap experiment. As in the case of that experiment, utmost care is required to eliminate uncertainties due to muon atomic physics effects. Thus, while the general experimental strategy is based on MuCap, a new cryogenic TPC operating at gas densities of 5% of LH_2 at 30 K will be developed to achieve optimal conditions for an unambiguous interpretation of the experiment. The TPC will be filled with ultrapure deuterium and operated as a high resolution ionization chamber. The different physics requirements of the new MuSun experiment demand several upgrades to the MuCap detector, including full analog readout of the cryo-TPC, the monitoring the muon chemistry by charged particle, neutron and γ detection and an advanced D_2 gas purification system.

Contents

1 Beam Requirements and Beam Request

Experimental Area:
πE3 equipped with a μ/e separator and the muon on request beam line setup using the MuLan kicker.

Required beam properties:

- Particle: μ^+, μ^-
- Momentum: 30 - 50 MeV/c
- Momentum width: 3% FWHM
- Beam spot: 5 cm diameter max
- Intensity: $\approx 10^5 s^{-1}$ (requiring normal high intensity ring operation)
- Beam purity: $\pi/\mu < 10^{-5}$,$e/\mu < 20\%$

Duration of experiment:
Based on the experience with the MuCap experiment we would ask PSI after discussion with other area users, specifically the μSR facility, to provide space for the MuSun apparatus to be permanently positioned inside the πE3 area. If this is not possible, we emphasise the absolute necessity of 6 weeks preparation time before a run in a suitable mounting space in the experimental hall ($\sim 20\ m^2$) due to the complexity of the setup before an experimental run.

- Preparation time in WEHA before first run 6 weeks;
- Test run with beam (5 weeks) in 2008;
- Engineering run and data taking (5 + 8 weeks) in 2009;
- Final production beam time is estimated to be 22 weeks.

Further requests will depend on the results of the test and engineering runs.

2 Questions of Safety

1. There is no dangerous radioactivity involved (only some calibration sources).
2. The TPC detector is an active target filled with deuterium gas (volume $\sim 20\ l$, pressure ≤ 10 bar at 30K). The usual hydrogen safety precautions shall be taken. The beryllium beam window is the weakest part of the hydrogen pressure vessel. It will be extensively tested during long term running.
3. The experiment will be operated in an air-conditioned climate tent with monitoring equipment for hydrogen, oxygen and flammable gases, similar to the equipment successfully operated over years within the MuCap experiment's climate tent.
4. Standard precautions for working with a cryogenic apparatus will be taken.

3 Physics Motivation

The MuSun experiment will measure the rate Λ_d for the semileptonic weak process

$$\mu^- + d \rightarrow \nu_\mu + n + n \tag{1}$$

to a precision of better than 1.5 %. Λ_d denotes the capture rate from the doublet hyperfine state of the muonic deuterium atom in its 1S ground state. The measurement, based on novel techniques, would exceed the precision of previous experiments by nearly an order of magnitude. Here, we summarize the primary physics motivation, while more details are provided in the next section.

- Muon capture on the deuteron is the simplest weak interaction process on a nucleus which can both be calculated and measured to a high degree of precision. The MuCap experiment, which published initial physics results [1] and successfully finished data taking in 2007, will determine the singlet capture rate Λ_S of the basic process on a free nucleon $\mu^- + p \rightarrow \nu_\mu + n$ to better than 1%; a prerequisite for precise calculations of muon capture. At the same time, modern effective field theories (EFTs) have been highly successful in calculating low-energy phenomena from first principles [2]. Reaction (1) could serve as a benchmark of our understanding of weak processes in the two-nucleon system. However, the best existing experiments [3, 4] are not precise enough and the most precise result differs from modern theory [5, 6] by 2.9 standard deviations.

- Reaction (1) is closely related to fundamental reactions of astrophysical interest. These include the $p + p \rightarrow d + e^+ + \nu_e$ reaction, which is the primary energy source in the sun and the main sequence stars, and the $\nu + d$ reaction, which provided convincing evidence for solar neutrino oscillation, as both its charged current and neutral current modes are observed simultaneously at the Sudbury Neutrino Observatory [7]. While the vector current interaction on the deuteron is scrupulously tested by a comprehensive set of experiments on electromagnetic observables, direct experiments on the axial-vector interaction with the two-nucleon system are scarce and have not come even close to the required precision. The above mentioned astrophysical processes responsible for the slow burning of the stars are simply too feeble to be observed in the laboratory. Here again, the development of EFTs during the last years has led to an important model-independent connection. It was proved that, up to the required precision in the systematic chiral expansion, these weak reactions are related by a two-nucleon current term, whose strength is parameterized by a single low-energy constant [8, 9, 5, 10, 11]. The constant integrates all the short-distance physics, which is not well constrained and considered the main theoretical uncertainty in these processes. The proposed MuSun experiment can determine this constant precisely from muon capture on the deuteron and thus comes closest to calibrating these basic astrophysical reactions under terrestrial conditions.

- The MuSun measurement is even more broadly related to different physics via EFTs. The low-energy constant representing the coupling of the axial current to the two-nucleon system resembles g_A in the one-nucleon sector. Analogously to the Goldberger-Treiman relation it relates the two-nucleon axial vector interaction to the coupling of a p-wave pion to two nucleons. For example, Ref. [12] points out that a precise measurement of $\mu + d$ capture will significantly reduce the uncertainty in the nn scattering length a_{nn}= 18.59 $\pm$ 0.27(exp) $\pm$ 0.30(theory) fm extracted from radiative pion capture $\pi^- + d \rightarrow \gamma + n + n$, by nearly eliminating the theory uncertainty. The difference between the pp and nn scattering lengths represents important data to quantify isospin symmetry breaking caused by the up and down quark mass difference in QCD.
  On a more methodological aspect, reaction (1) will allow a detailed comparison with existing calculations [13], where the critical $2N$ axial current is determined from the more complex three-nucleon system (tritium beta decay). Such a calculation can currently only be performed in a hybrid approach (using phenomenological wave functions), whereas the $2N$ system can be successfully treated within a fully consistent chiral perturbation theory framework. There is considerable practical interest in the verification of the reliability of the hybrid approach, which does not follow the strict chiral order counting, but is applicable in a wider range of few-body systems, like, e.g., the solar hep reaction [14], which is notoriously difficult to calculate.

4 Muon Capture on the Deuteron

4.1 Theoretical Framework

During the last decade, effective field theories (EFTs), especially chiral perturbation theory (ChPT), have been used as a natural theoretical framework for calculating weak processes on a single nucleon, the deuteron and even the three- and four-nucleon systems. ChPT inherits the relevant symmetries of QCD and its parameters are linked to matrix elements of QCD operators. At sufficiently low energy-momentum transfer, there has been tremendous theoretical progress, with strong experimental confirmation, in applying EFTs to a variety of observables in the one-nucleon sector .

As developed in the pioneering work of Weinberg [15, 16, 17], one can construct an EFT applicable to multi-nucleon systems. All EFTs rely on an expansion scheme in a small parameter $Q/\Lambda \ll 1$, where Q is the four-momentum of the relevant process and Λ indicates the relevant mass scale. The expansion is in powers of Q/Λ, where the higher order terms give smaller corrections to the dominant lowest order terms. The *effective* nature of EFT is reflected in the presence of unknown coefficients, called the low-energy-constants (LECs), which parameterize the high-energy physics that, in generating the low-energy EFT, has been integrated out. In principle these LECs can be evaluated from QCD, but in practice they are determined from experimental data. Once the LECs are determined, the theory will make unambiguous predictions of observables for many different processes. For example, the $\mu^- + p$ capture rate has been evaluated including one-loop corrections, a level of precision that includes several LECs which are determined empirically from other reactions [18]. The pseudo-scalar constant g_P, linked to the pion pole contribution in $\mu^- + p$ capture, is evaluated to high precision in ChPT which gives an expression for g_P in terms of the fundamental LECs, f_π and g_A and the nucleon axial radius, which are known.

In the pion-less EFT (where the pion is considered a high-energy degree of freedom and has been integrated out) the expansion parameter is $Q/m_\pi \ll 1$, where Q is a typical energy or momentum of the reaction and m_π is the pion mass. In ChPT, on the other hand, the expansion parameter is $Q/\Lambda_\chi \ll 1$, where $\Lambda_\chi \simeq 4\pi f_\pi \simeq m_N$ with m_N the nucleon mass. At very low energies ($Q \ll m_\pi$) the pion-less EFT ($\not\pi$EFT) is very useful. However, for $\mu^- + d$ capture $Q \simeq m_\pi$. Therefore ChPT, which is valid over a much larger energy-momentum region, is the better theory in this case. This conclusion is also obvious from Fig. 1, which shows the entire phase space available for $\mu^- + d$ capture. The $\not\pi$EFT applies only in the bottom left part of the figure, as indicated[1]. In contrast, ChPT is valid for the entire phase space, with some modifications perhaps needed in the region closer to the $p_\nu = 0$ point, where the momentum transfer becomes large. However, as shown in Ref. [5], the contribution from this region to the total capture rate is marginal. Also, due to the larger range of allowed energies, ChPT applies to more processes than $\not\pi$EFT.

At the desired level of precision the two-nucleon ($2N$) system has one new unknown LEC characterizing the short-distance $2N$ axial current. This LEC is called L_{1A} in the pionless theory [6] and $\hat{d}^R$ in ChPT [5]. In the latter case the pion-exchange currents between the $2N$s are explicitly evaluated, while they are embedded in L_{1A} in the $\not\pi$EFT. The coupling constant $\hat{d}^R$ enters in a range of important weak and pionic reactions, e.g., $\mu^- + d$, $p + p$ fusion [13], $\nu + d$ reactions [19], and pion radiative capture on the deuteron [12]. At present, $\hat{d}^R$ is determined from triton beta decay using so-called hybrid ChPT (employing phenomenological wave functions). Theoretically it is highly desirable to determine its value within the $2N$ system and in a consistent ChPT framework. Once $\hat{d}^R$ is determined in this way, the solar $p + p$ fusion and νd SNO reactions will be determined in a model independent way at the same precision as the measured $\mu^- + d$ capture reaction. Recent developments have also made it possible to derive the deuteron and scattering state wave functions within chiral perturbation theory [20, 21, 22, 23, 24, 25], without having to resort to the hybrid approach. Thus all the relevant $2N$ processes can be calculated ab-initio entirely within the same consistent framework.

[1] Experimentally we could determine the reduced capture rate for this region of $p_\nu \geq 90$ MeV/c by measuring both the total capture rate and the higher energy Dalitz plot region by detecting neutrons with energies above 10 MeV. We are evaluating the overall physics motivation for such an expansion of the experiment, but that would be a separate proposal.

4.2 Capture Rate Calculations, Status and Future

Compared to the elementary $\mu^- + p$ capture, several additional features are important in the $\mu^- + d$ capture process. The properties of the $2N$ system enter, in particular the deuteron wave function in the initial-, and the neutron-neutron scattering length a_{nn} in the final state. The above mentioned two-body axial currents contribute, making process (1) uniquely suited to study them in the $2N$ system. The final three-body state allows a broad range of momentum transfer to the $2N$ system (see Fig. 1). The total energy $Q = 102.1$ MeV in the final state, adequately described in non-relativistic kinematics, is the sum of the neutron CMS energy, two neutron relative energy E_{nn}, and the neutrino momentum p_ν.

$$Q = \frac{p_\nu^2}{4M_n} + E_{nn} + p_\nu. \tag{2}$$

Thus the kinematics can be parameterized either by E_{nn} or equivalently by p_ν.

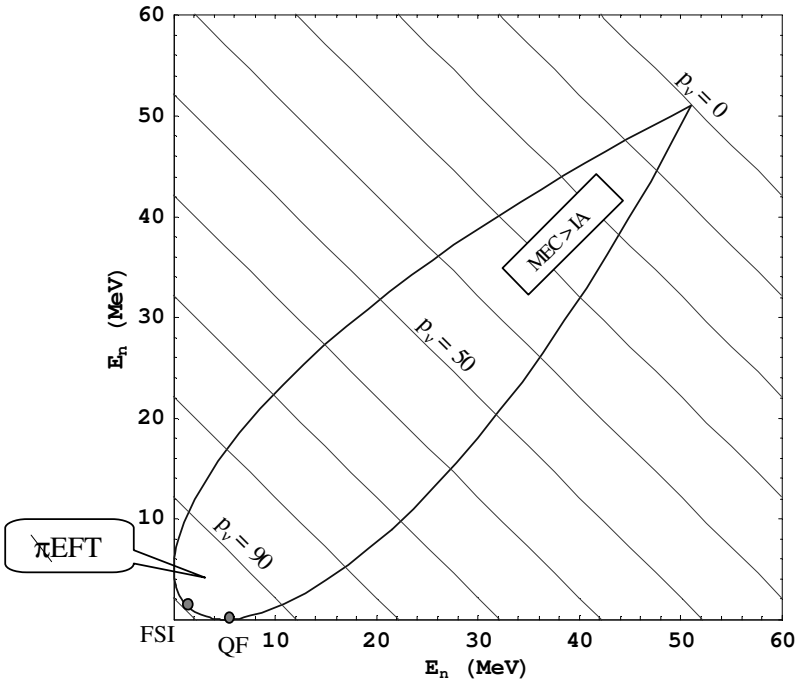

Figure 1: $\mu^- + d$ capture Dalitz plot as function of the neutron kinetic energy. Diagonal lines indicate constant neutrino momentum p_ν (MeV/c). Some interesting kinematic regimes are marked in the graph: final state interaction (FSI); quasifree (QF); $p_\nu \geq 90$ MeV/c, where pion-less EFT applies; small p_ν, where MECs dominate over impulse approximation.

Traditionally, muon capture has been calculated in the standard nuclear physics approach, essentially an impulse approximation calculation based on realistic nucleon-nucleon potentials supplemented by explicit models of the two-body meson exchange currents. The most sophisticated of these calculations were performed around 1990 [26, 27, 28]. Thereafter the concept of effective field theories in the form of ChPT was expanded to the $2N$ system. The latest calculations were performed in hybrid EFT [5] and most recently in $\not\pi$EFT [6]. Figure 2 summarizes the theoretical and experimental results.

Present calculations agree that the one-body operators are very well defined. The challenge lies in the short range part of the axial two-body current. In the meson exchange picture, it is dominated by the πNN^* isobar current, which is not constrained by general symmetry principles. The systematic expansion of ChPT demonstrates that exactly the same combinations of low energy constants appear in the two body reactions $p + p$ fusion, $\nu + d$ scattering and $\mu^- + d$ capture. The hybrid EFT used tritium beta decay to constrain the unknown LEC. The $\not\pi$EFT treats this LEC, called L_{1A}, as an unknown parameter and parameterizes the capture rate as

$$\Lambda_d = a + b\ L_{1A} \tag{3}$$

where a and b weakly depend on the E_{nn} Dalitz plot cut, provided E_{nn} is limited to the kinematic region where $p_\nu < 90$ MeV/c. For $E_{nn} = 5$ MeV, a=239.2s^{-1}and b=3.3s^{-1}fm^{-3}. The currently best estimate of L_{1A} depends on hybrid ChPT calculations [6], see also Table 2. The hybrid ChPT calculation [5] obtains Λ_d= 386 s^{-1} and estimates an uncertainty of 1%, resulting from a small dependence on the cutoff parameter, uncertainties in the tritium beta decay rate [13], higher MEC contributions and a phenomenological estimate of the contribution of the $L \geq 1$ partial waves [26]. Reference [5] also notes that radiative corrections still need to be calculated. The ⧸πEFT paper concludes that its uncertainty of 2-3% is dominated by N^{3}LO contribution, not yet calculated [6]. However, it would still rely on hybrid ChPT for a precise value for L_{1A}.

As mentioned above, the theoretical program supporting the MuSun experiment plans to calculate $\mu^- + d$ ab-initio in a fully consistent approach, where both the $2N$ wave functions and the operators are derived within the recently developed ChPT framework. An advantage over the present ⧸πEFT calculation is that the relevant kinematic range of the reaction is fully within the convergence radius of the theory and that the higher order effects are estimated to contribute less than 0.5%.

At the level of precision aimed at in the proposed $\mu^- + d$ capture experiment, an evaluation of the radiative corrections will be necessary. Traditionally, the evaluation of radiative corrections for a nucleon is based on either the quark picture or the pre-EFT hadronic picture. In the former, the calculation is well defined at the quark-lepton level [29, 30]. Meanwhile, calculations based on the pre-EFT hadron picture involve intrinsic model dependence. ChPT provides a reliable systematic framework which respects all required symmetry properties and wherein one can enumerate and evaluate all the relevant Feynman diagrams up to a specified chiral order (see, e.g., [2]). The ChPT evaluation of radiative corrections of neutron β-decay was developed in Ref. [31], and this formalism can readily be applied to $\mu^- + p$ capture. This treatment involves unknown LECs associated with photon loops. These LECs are constrained using the high-precision data on neutron β-decay and can then be used in $\mu^- + p$ capture. Furthermore, ChPT can be applied in the calculations of $\mu^- + d$ radiative corrections.

4.3 Experiment

The early counter experiments were based on the observation of capture neutrons. While a precise measurement of the absolute neutron emission rate is difficult even for 5.2 MeV neutrons resulting from $\mu^- + p$ capture, it is even harder for the continuous spectrum of neutrons emitted in $\mu^- + d$ capture which is peaked around 1.5 MeV. Moreover, numerous 2.45 MeV neutrons are produced by muon-catalyzed dd fusion, representing a significant background. The interpretation of the experiments requires an accurate knowledge of $d\mu^-$ hyperfine population at the moment of capture, because the V-A structure of weak interactions suppresses capture from the quartet relative to the doublet state. The first generation experiments [32, 33] tried to reduce the background from dd fusion, by using hydrogen targets with small deuterium concentration. Because of the fast $p\mu^-$ to $d\mu^-$ transfer rate, such a target acts as an effective deuterium target. The price to pay for such an approach is that at high densities capture occurs from a molecular state and the background from μ^3He build-up is significant. For lower densities, on the other hand, the $d\mu^-$ hyperfine population was essentially unknown at that time and was conjectured as being pure doublet.

Ref.	ϕ(%)	c_D(%)	T (K)	detection	statistics	Λ_d(s^{-1})
[32]	100	0.32	20	neutron	615	365±96
[33]	0.76	5	300	neutron	6295	? *)
[3]	100	100	20	electron	5×10^8	470±29
[4]	4	100	45	neutron	≈ 9000	409±40

Table 1: Experiments on $\mu^- + d$ capture. Density ϕ normalized to LH_2 density. Experiments performed in D+H mixtures, with c_D given in column 3. *) Result uncertain, because experimental conditions corresponds to mostly statistical, not doublet dμ^- hyperfine population, as originally assumed.

The situation changed with the discovery [34] of a strong temperature dependent hyperfine effect in resonant $dd\mu^-$ formation, which made the $d\mu^-$ hyperfine population directly experimentally accessible. This and subsequent experimental and theoretical work showed that the conditions in experiment [33] were closer to statistical, than doublet. As a consequence the reported experimental rate of Λ_d= 445±60 s^{-1} would have to be corrected upwards by a factor of up to three, according to the weight

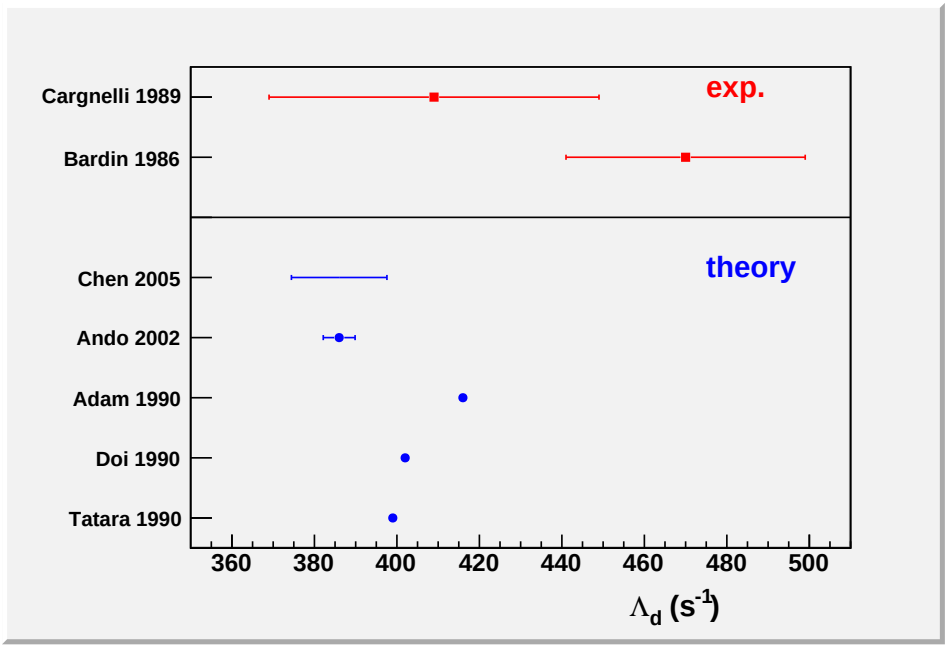

Figure 2: Recent theoretical and experimental results on Λ_d. The theory improvements due to the EFT method are evident. For the first time systematic theoretical error estimates are provided. The calculation of Ando 2002 [5] claims an uncertainty of 1%, albeit based on a hybrid calculation. The error range for the pion-less EFT calculation of Chen 2005 [6], applicable to the low momentum transfer region, includes the estimated uncertainty of uncalculated chiral orders. For the value shown in the figure, L_{1A} was adjusted to reproduce the rate of Ando et al. In the near future, Λ_d will be calculated with half the uncertainty of Ando 2002, i.e. 0.5%, based on a fully consistent ChPT formalism. This precision level is the challenge for the new MuSun experiment.

of the μd doublet state in the statistical mixture. The resulting contradictory situation stimulated a new generation of experiments based on pure deuterium targets.

One innovation [3] was the detection of electrons with a liquid target at Saclay, which avoided neutron detection and background from dd fusion. Lifetimes of both μ^- and μ^+ were measured with an accuracy of a few times 10^{-5}. The muon lifetime measurement started 1 μs after the beam burst, after muons stopped in wall materials were already captured. The final rate included a corrections of $\Delta\Lambda_d = 12$ s^{-1} for protium (c_P=0.13-0.18%) and of $\Delta\Lambda_d = (60 \pm 16)$ s^{-1} for μ^{-3}He capture. The total uncertainty quoted is ± 29 s^{-1}, corresponding to ± 25(stat) and ± 16(sys) s^{-1}.

The Vienna PSI experiment [4] on the other hand used neutron detection, but reduced the gas density and temperature to suppress fusion neutrons and performed supplemental analyses with high neutron threshold above the 2.5 MeV fusion neutrons. In the low density target the stopping fraction of muons in D_2 was (75.7 ± 1.7)%. The physics background, consisting of carbon stops, diffusion, photo neutrons and fusion neutrons, exceeded the physics signal by a factor of 1.4. The uncertainties in its subtraction dominated the averaged final error of ± 40 s^{-1}, with statistics and uncertainty in neutron detection efficiency contributing ± 15 and ± 20 s^{-1}, respectively.

The current overall experimental situation on Λ_d (see Fig. 2) is quite unsatisfactory. The best two measurements were performed almost two decades ago. They have uncertainties of 6.2-10% and are only marginally consistent, with the more accurate experiment deviating from theory by 2.9 σ.

4.4 Connections to Neutrino and Astrophysics

As mentioned in the introduction the reactions

$$p + p \rightarrow d + e^+ + \nu_e \quad (4)$$

$$\nu_e + d \rightarrow e^- + p + p \quad (5)$$

$$\nu + d \rightarrow \nu + p + n \quad (6)$$

are of fundamental physics interest. Reaction 4 is the primary solar fusion process which is one of the key inputs that controls the solar model. Reactions 5, 6 are the charged and neutral current reactions (CC, NC) detected by SNO and their comparison provides direct evidence for neutrino oscillation and the NC process serves as the measurement of the total ^{8}B neutrino flux from the sun [35]. As these processes have eluded quantitative measurements, there has been a tremendous theoretical effort to calculate them with ever increasing precision. Let us focus on the $\nu + d$ reaction. Up to 2001, the calculations [9] were performed within the standard nuclear physics approach, where two body-current effects were estimated from two experimental sources, namely the tritium beta decay rate Γ^β and the $n + p \to d + \gamma$ cross section. The results of the two methods differed by 3%, which was adopted as the theoretical uncertainty. In 2002 these results were updated [36] and the uncertainty estimate reduced to 1% by arguing that the $n + p \to d + \gamma$ constraint should be discarded, because it refers to a vector transition only. In 2003 these calculations were corroborated by the above mentioned EFT inspired hybrid approach [10], which uses phenomenological wave function together with EFT derived operators and again employs Γ^β to control the $2N$ part. The hybrid approach is, in principle, subject to criticism concerning consistency in chiral power counting, off-shell ambiguities etc., although these effects are estimated to be small [13]. Possible approaches that are formally consistent are the $\not\pi$EFT [37] and ChPT. Both these approaches, however, are not predictive, as the missing LECs L_{1A} and $\hat{d}^R$, respectively, are not determined at this point. Very recently, a model dependent analysis of low energy νd cross sections has estimated the νd cross sections to be accurate to 2–3% [38].

The SNO experiment [35] has adopted a 1.1% uncertainty in the cross sections used in their data analyses to determine the ^{8}B neutrino fluxes. In view of the discussion above this appears optimistic and basically rests on validity of the hybrid approach at this precision level.

As regards the *pp* fusion process, the situation is similar. The standard solar model [39] adopts a 0.4 % uncertainty in the *pp* S-factor, in accordance with a standard nuclear physics [40] and hybrid EFT calculations [13], both relying on the Γ^β constraint. These considerations make assumptions regarding the dynamics of the three-nucleon system which can be avoided if we stay completely within the two-nucleon sector.

	method	L_{1A} (fm^3)	comment
two-body			
	reactor $\bar{\nu} + d$	3.6 ± 5.5 [11]	i)
	ES, CC, NC in SNO	4.0 ± 6.3 [41]	ii)
	MuSun proposal	**±1.25**	
three-body			
	tritium beta decay	4.2 ± 3.7 [11], 4.2 ± 0.1 [41]	iii)
other			
	helioseismology	4.8 ± 6.7 [42]	iv)

Table 2: L_{1A} determinations compiled in Refs. [11, 41]. The only theoretical clean and fully self-consistent calculations can be performed in the 2-nucleon system, where the MuSun experiment will have a major impact. The L_{1A} determination from tritium decay claims high accuracy, but the extraction can only be done in the hybrid EFT approach with phenomenological wave functions in the more complex three-body system. i) The best experiment determines L_{1A} to ± 8.1 fm^3 only. The averaging procedure is questionable as indicated by the small global χ^2; ii) the error is expected to be reduced to $\sim 5 fm^3$ with the final SNO data; iii) Ref. [11] includes the uncertainty in higher-order theoretical systematics, while Ref. [41] does not, which leads to the large difference in the error estimate for L_{1A} ; iv) subject to other solar model uncertainties.

In view of the importance of these cross sections and the ongoing discussion described above, several attempts have been made to fix the $2N$ contribution independent of Γ^β. These efforts can be conveniently parametrized in terms of the LEC L_{1A} and in the future with $\hat{d}^R$, which is more appropriate if one also includes muon capture (c.f. table 2). MuSun will lead to a decisive improvement, using information solely from the theoretically clean two-nucleon sector.

Refs. [44, 43] study how the solar neutrino mixing parameters vary with the assumed value of L_{1A}. Figure 3 shows that there are subtle but nevertheless visible changes in the $(\theta_{12}, \delta m^2_{21})$ exclusion regions as L_{1A} is varied over its plausible range from 0 to 10 fm^{-3}. These changes primarily correspond

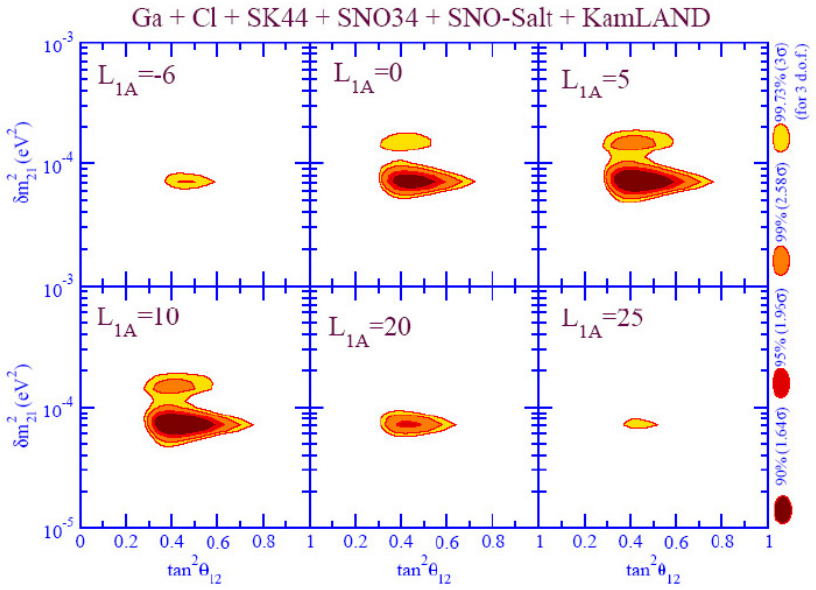

Figure 3: Dependence of solar neutrino mixing parameters on assumed value of L_{1A}. Reproduced from [43].

to a uniform reduction in the fit probability, as the solar neutrino data becomes less self-consistent for extreme values of L_{1A}. The authors' conclusion is that the uncertainty in the solar neutrino mixing parameters from L_{1A} is somewhat smaller than that arising from θ_{13}. However, as we enter a phase of precision neutrino physics, several current uncertainties will be tightened by future experiment, enhancing the importance of L_{1A}. As examples the uncertainty in θ_{13} will be reduced to the sub-percent level and the final SNO-III phase [45] is expected to reduce the total experimental uncertainty in the charged-current flux from 6.3 % to 4.0 %, which is comparable to the theoretical uncertainties discussed above. An updated analysis along the lines of Refs. [44, 43] would be very interesting, which includes constraints from future neutrino experiments and also the effect of L_{1A} on the ^{8}B (and *pp*) flux within the standard solar model. As regards the solar *pp* neutrino flux, the solar luminosity constraint strongly reduces its sensitivity to the *pp* cross section. For constraining alternate fusion sources in the sun or testing, whether the sun is in a steady state, or calculating the ^{8}B flux, improved knowledge of the *pp* reaction is more than a symbolic achievement. Finally, studying few-nucleon systems also helps us to improve our understanding of electroweak phenomena in more complex nuclei, which feature in a wide variety of astrophysical phenomena including neutrino-nucleosynthesis.

4.5 Other Physics Connections

Nuclear Physics

As already mentioned, the LEC $\hat{d}^R$ also connects $\mu^- + d$ capture to $\pi^- d \to \gamma nn$. This radiative pion capture process is considered to be the most reliable (experimentally and theoretically) method of extracting the nn scattering length (a_{nn}) [46], while the alternative method of using the three-nucleon process $nd \to nnp$ is plagued with inconsistent results [47, 48]. The difference of the nn and pp scattering lengths is used to constrain the charge-symmetry-breaking pieces of the modern high-precision phenomenological nucleon-nucleon potentials, which in turn are needed for detailed understanding of the lighter nuclei ($A < 20$) [49, 50]. The theoretical error in a_{nn} extracted from $\pi^- d \to \gamma nn$ can with ChPT methods be reduced to ± 0.05 fm, i.e., to the 0.3% level [21, 12, 51]. However, this precision can be reached only if the short-range physics is constrained by $\hat{d}^R$. Thus a precision measurement of $\mu + d$ would also help in establishing a precise value of a_{nn} completely within the two-body sector and ChPT.

Hydrogen TPCs

With the MuCap TPC and the MuSun cryo-TPC we will have developed a range of high-density, thin walled time projection chambers covering an equivalent pressure range of 5-100 bar at room temperatures. The chambers operate with ultra-pure hydrogen at a purity level of ppb. The MuCap TPC operates at lower pressure with gas amplification. The MuSun TPC will be a cryo ionisation chamber with full analog readout and excellent energy resolution. As hydrogen and deuterium are basic target elements, these new instruments might find interesting applications in nuclear/particle physics. In the realm of muon physics, we are considering future experiments on the hep process and on rare fusion reactions of astrophysical interest.

4.6 Extraction of (L_{1A}, $\hat{d}^R$) from $\mu + d$ Capture

We have already made the more general statement that the solar $p+p$ fusion and νd SNO reactions will be determined in a model independent way at the same precision as the measured $\mu^- + d$ capture reaction.

Here we use Eq. 3 for estimating more specifically how the Λ_d measurement can determine L_{1A}. Equivalently, we use L_{1A} as a convenient device to estimate how different uncertainties affect the $\mu^- d$ capture rate. The discussion could equally be framed in terms of $\hat{d}^R$, as the Λ_d dependence on $\hat{d}^R$ is well approximated by a linear relation, equivalent to Eq. 3. Simple error propagation leads to

$$\delta L_{1A} \approx \frac{a}{b} \frac{\delta \Lambda_d}{\Lambda_d} \tag{7}$$

The fractional uncertainty $\frac{\delta \Lambda_d}{\Lambda_d}$ consists of the measurement error (1.2%) and a theoretical uncertainty. The latter consists of an estimated uncertainty of 0.5% in the ChPT calculation and an uncertainty introduced using g_P from the Λ_S measurement (0.7%). The dependency on the neutron scattering length a_{nn} leads to $\frac{\delta \Lambda}{\Lambda} = 0.9\%$, if the currently accepted value of $a_{nn} = -18.6 \pm 0.4$ fm is being used. Together these add up to

$$\frac{\delta \Lambda_d}{\Lambda_d} = \pm 1.7\% = \pm 1.2\%(exp) \pm 1.25\%(theory) \tag{8}$$

The resulting precision in L_{1A}= 1.25 fm^3. If only an overall $\frac{\delta \Lambda_d}{\Lambda_d}$ of 2% is obtained, the uncertainty in L_{1A} would increase to 1.5 fm^3, still far better than any other 2-body information in table 2.

4.7 Muon Capture, the Big Picture

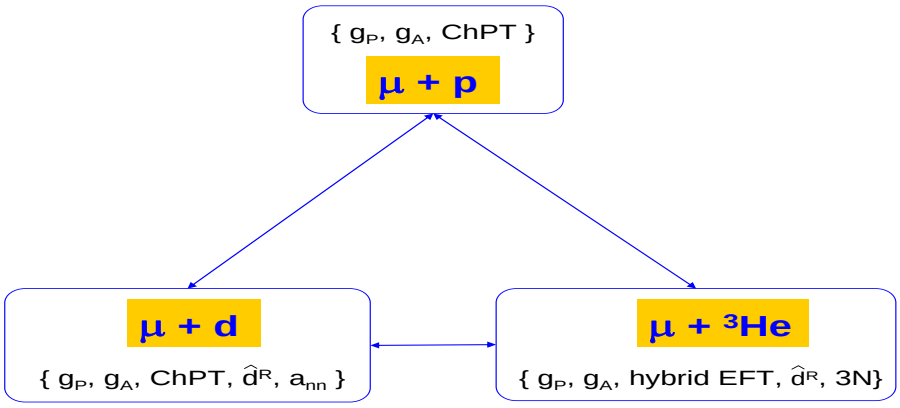

Figure 4: Relations between basic muon capture reactions on the nucleon and A = 2, 3 nuclei. This is further discussed in the text.

The MuSun experiment is part of our systematic program to achieve a new level of precision in confronting the theories of weak interactions, QCD and few body physics with precision muon capture

experiments on $\mu^- + p \rightarrow \nu_\mu + p$, $\mu^- + d \rightarrow \nu_\mu + n + n$ and $\mu^- + {}^3\mathrm{He} \rightarrow \nu_\mu + t$. We limit the discussion to these three cases, as the nuclear physics of nuclei with A>3 becomes increasingly difficult to control at the required precision level, notwithstanding the significant progress achieved recently in this field. Moreover, it is clear that the understanding of the basic reactions above is required for predicting muon capture observables in heavier nuclei.

The different parameters and theories relating the above three muon-capture reactions are illustrated in Fig. 4. As is typical for EFTs, many LECs are determined already in the single-nucleon system and carry over unchanged when more nucleons are added. However, in the two-nucleon system, there appear two new parameters, i.e., $\hat{d}^R/L_{1A}$ and a_{nn}, both of which are well defined and can be determined precisely. The one- and two-nucleon systems can be treated entirely within the framework of ChPT, but when going to three nucleons, the currently only available option is to use phenomenological wave functions, i.e., hybrid ChPT. The three-nucleon system also introduces additional LECs and the complications of three-body dynamics.

Quantities like g_A, g_P and $\hat{d}^R/L_{1A}$ encode basic properties of the nucleon or two-nucleon system, when interacting with the axial-current. They are equally important as indispensable input to precision calculations. For example, g_A is needed for all calculations of weak Gamow-Teller transitions, g_P quantitatively tests our understanding of basic QCD symmetries and $\hat{d}^R/L_{1A}$ allows the calculation of immeasurable and fundamental neutrino processes.

From the modern nuclear physics perspective, the triad of muon capture experiments is an important component of a main thrust to derive nuclear physics from QCD. This worldwide effort utilizes different probes to precisely determine the low-energy constants and test the internal consistency of the theory. As just one example, it is expected that the new generation of neutron decay experiments will resolve the current controversy on the neutron lifetime and g_A. Before our program started at PSI, muon capture was hardly a contender in this worldwide effort, as the experimental precision was not competitive. This has changed dramatically during the last decade.

Our first experiment [52] on $\mu^- + {}^3\mathrm{He} \rightarrow \nu + t$ achieved a precision of 0.3%, unique in this field of physics and equal to the precision of the tritium decay rate [53]. Efforts to achieve similar precision theoretically are still ongoing and, recently, a calculation of radiative corrections [30] revised the elementary particle model calculation, which was previously considered to be very accurate, by 3%. The analyses of a first data set [1] on $\mu^- + p \rightarrow \nu + n$ achieved a first precise result on g_P, nearly independent from the uncertainties from muonic molecule formation, which have plagued earlier experiments for many years. The final result on the capture rate Λ_S is expected to have <1 % uncertainties and will establish a critical test of a basic ChPT prediction, where g_P is an accurately defined derived quantity. At this level the extraction of g_P would be affected by the new neutron lifetime experiment [54], which, if taken as the new standard, would imply a $\approx 0.8\%$ shift in the theoretical prediction for Λ_S. The new MuSun experiment will be the cleanest way to determine $\hat{d}^R/L_{1A}$ required for precision calculations of basic astrophysical reaction and will shed light on the precision of ChPT versus hybrid EFT, relevant for many reactions.

Once this experimental program is completed, we plan a combined, consistent analysis of our results on all three reactions using the best theoretical input available at that time [2].

5 Experimental Strategy

5.1 Overview

In order to achieve the goal of this experiment two main conditions have to be met.

- The measurement must be performed at conditions, such that the experimental result leads to an unambiguous extraction of Λ_d, independent from muonic atomic physics uncertainties.
- The measurement must achieve an overall precision of 1.5 % or better of Λ_d (6 s^{-1}), which is nearly an order of magnitude higher than achieved in previous experimental work.

[2] Depending on the evolving overall picture, we will then assess whether additional dedicated, but very difficult experiments of polarization observables in muon capture are justified, where the $\mu^- + d$ is a promising candidate.

Muon Kinetics and Optimal Target Conditions

The muon induced atomic and molecular processes (*muon kinetics*) are quite different for negative muons in deuterium compared to the muon kinetics in pure protium (relevant for the MuCap experiment). The hyperfine transition rate λ_{qd} of the upper $d\mu(\uparrow\uparrow)$ quartet to the $d\mu(\uparrow\downarrow)$ doublet state is slow. The V-A structure of weak interactions, however, disfavors capture from the quartet state (Λ_q=12 s^{-1}) compared to capture from the doublet state (Λ_d=386 s^{-1}), so that the experimentally observed capture yield is largely proportional to the population of the doublet state. The $d\mu$ system has been intensively studied as the prototype for resonant muon-catalyzed fusion [55]. For a clear interpretation and for the accumulation of sufficient capture statistics, the target conditions should be chosen such that the $d\mu$ doublet state dominates and the population of states can be verified *in-situ* by the observation of muon-catalyzed fusion reactions. Our optimization indicates excellent conditions at $\phi = 5\%$ of liquid hydrogen density and T=30 K, which we define as the baseline of the experimental proposal. On the positive side, complications from muon capture in the $dd\mu$ molecule are nearly absent, as it is short lived. Moreover, the pronounced $\mu d + p$ diffusion problem does not exist like in the case of the MuCap protium measurement, as the elastic cross section for $\mu d + d$ scattering is large. However, μ^3He formation, isotopic purity, and chemical impurities still need careful attention. Different from the isotropic decay from the singlet μp state in MuCap, the μ doublet and quartet state can remain polarized, which might lead to a time dependent decay asymmetry (c.f. appendix 11.1).

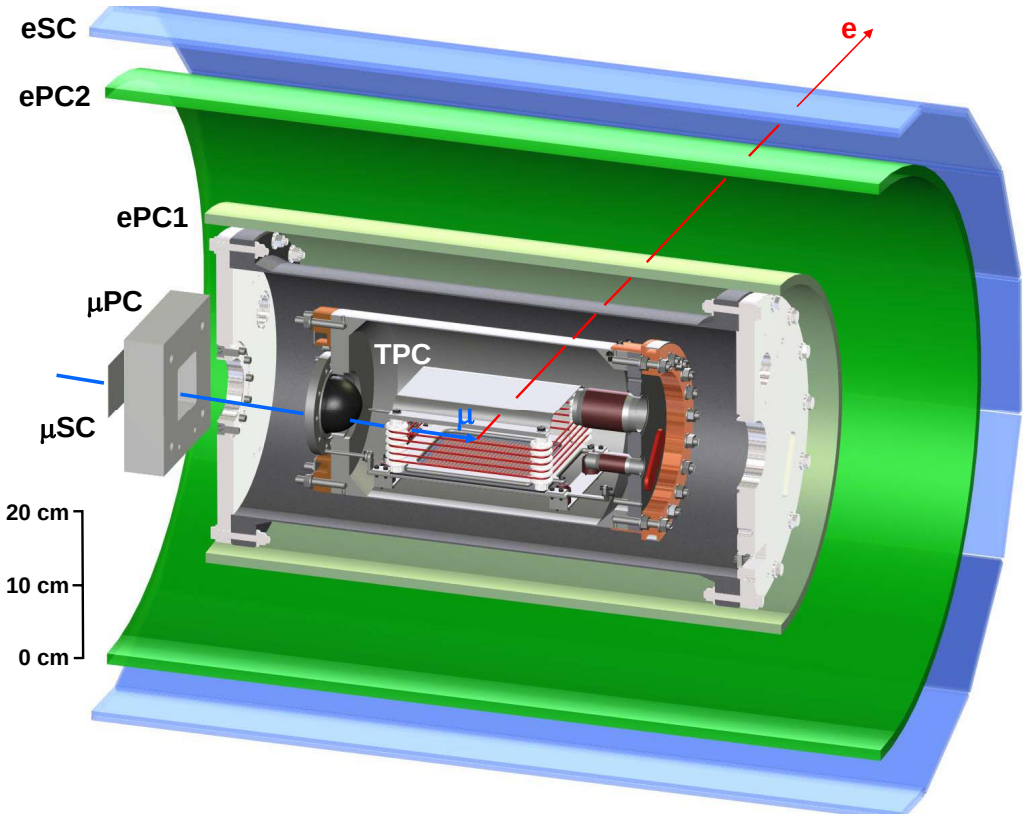

Figure 5: Simplified cross-sectional diagram of the MuSun detector. The detector components are described in the text.

Experimental Technique for $< 1.5\,\%$ Measurement

The gain in experimental precision relies on the fundamental techniques developed for MuCap. Muons will be stopped in an active gas target consisting of a cryogenic ionization chamber operated as time projection chamber (TPC or cryo-TPC) with chemically and isotopically ultra-pure deuterium. The reconstruction of the muon stopping point in 3 dimensions eliminates the otherwise overwhelming background from muon stops in wall materials. The capture rate is determined using the lifetime technique; that is, from the difference between the measured disappearance rate $\lambda_\mu^- \approx \lambda_\mu^+ + \Lambda_d$ of negative muons in hydrogen and the μ^+ decay rate λ_μ^+, where it is assumed that free μ^- and μ^+ decay with identical rates according to the CPT theorem.

The experimental setup is illustrated in Fig. 5. Incident muons first traverse a plastic scintillator (μSC) and a multiwire proportional chamber (μPC), and then pass through a 150 μm kapton window into the insulation vacuum and second, a 0.4-mm-thick hemispherical beryllium window to enter an aluminum pressure vessel filled with ultra-pure, deuterium gas at a pressure of 0.5 MPa and 30 K temperature. In the center of the vessel is the cryo-TPC (sensitive volume $10 \times 10 \times 10$ cm^3), which tracks incoming muon trajectories and thus enables the selection of muons that stop in the gas at least 5 mm away from chamber materials. Monte Carlo simulations indicate that approximately 85 % of the muons passing through the μSC stop within this fiducial volume. The ionization electrons produced by incoming muons drift downwards at velocity 4 mm/μs in an applied field of 10 kV/cm, towards a multi-pad plane of the cryo-TPC. Signals from the cryo-TPC are recorded deadtime free with custom build FADCs. The chamber is surrounded by two cylindrical wire chambers (ePC1, ePC2), each containing anodes and inner/outer cathode strips, and by a hodoscope barrel (eSC) consisting of 16 segments with two layers of 5-mm-thick plastic scintillator. This tracking system detects outgoing decay electrons with 3π solid angle acceptance. All data are recorded in a trigger-less, quasi-continuous mode to avoid deadtime distortions to the lifetime spectra.

The MuSun technique heavily builds on the R&D, equipment investments, techniques and analysis refinements developed for the MuCap and μLan experiments. The electron tracking system, the beam counters, the sophisticated vacuum and purification system and a large part of the electronics and data acquisition can be taken over from the MuCap experiment. The fast electric kicker, crucial for achieving pile-up free high event rates, and custom build FADCs are provided from the μLan experiment. The main distinctive features of the MuSun experiment are demanded by physics requirements and include:

- High density cryogenic ionization chamber operating as a TPC filled with ultra-pure deuterium to define the muon stop, identify impurities and to observe muon induced processes.
- Excellent energy resolution of the cryo-TPC and full analog readout with FADCs to monitor the charged particles induced by fusion and impurity capture processes.
- Advanced purity monitoring system with new particle detectors and chromatographic methods.
- Neutron detectors to monitor the muon kinetics via capture neutrons and fusion products and separate impurity from fusion signals in the TPC.

5.2 Kinetics

Fig. 6 shows a simplified scheme of the muon induced kinetics in pure deuterium[3]. Because of its unique importance for understanding muon-catalyzed fusion, resonant molecule formation, and weak interactions, this reaction chain has been scrupulously studied both experimentally and theoretically. The latest experimental results are presented in Ref. [56] which also includes many experimental details relevant for the present proposal. The current knowledge of the relevant parameters is compiled in Fig. 7 and Table 3. As is conventional, all density dependent kinetic rates have been normalized to LH_2 density N=4.25 $\times$ 10^{22} atoms/cm^3, and the density ϕ is expressed relative to this value.

[3]The simplifications include: The effective ddμ fusion rate has been omitted, since it is nearly instantaneous ($\leq$ 1 ns) at the time scales considered. The hyperfine state dependence of the branching ratio β has been ignored. Small corrections to the kinetics are induced by the finite thermalization time of μd atoms.

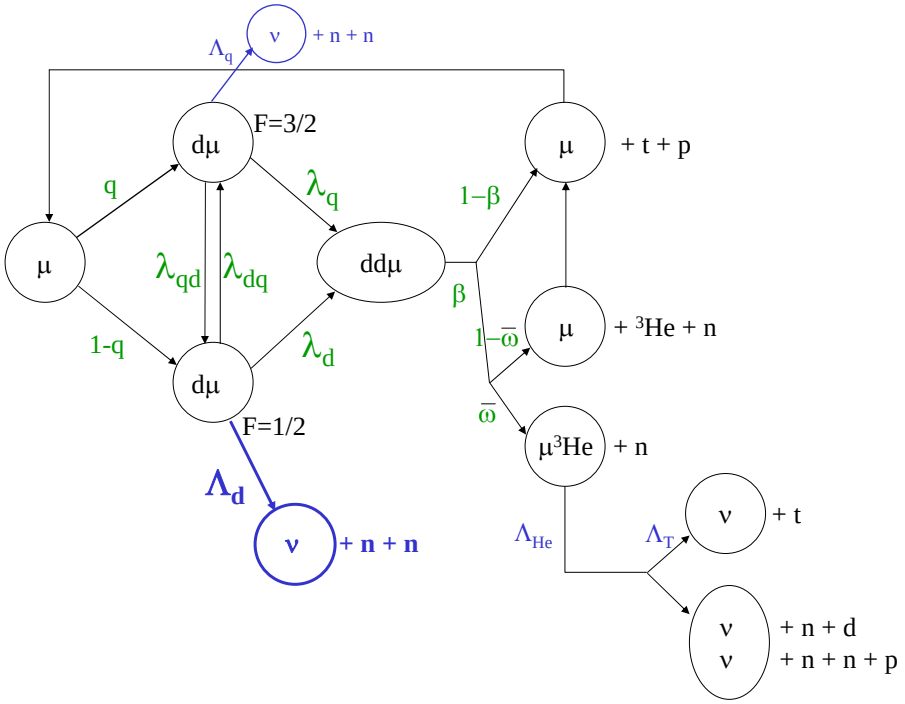

Figure 6: Simplified muon kinetics in pure D_2.

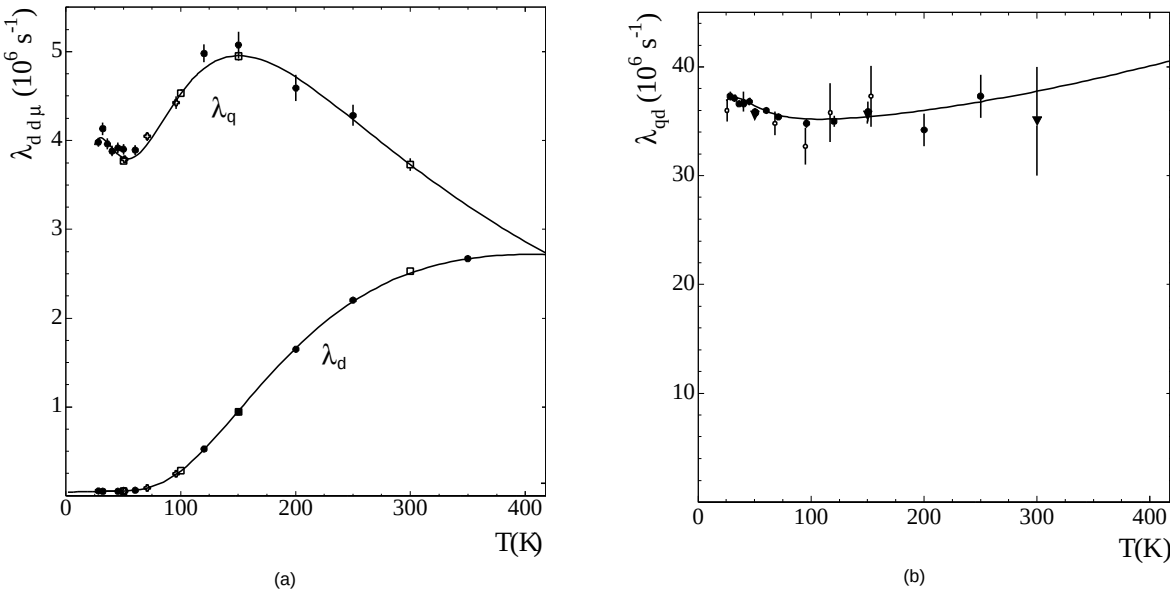

Figure 7: (a) Molecular $dd\mu$ formation rates λ_q and λ_d and (b) the hyperfine transition rate λ_{qd}. The experimental data comes from [56, 57, 34, 58]. For both panels, the plots are taken from [56] with some slight modifications.

description	quantity	value	
		300K	30K
initial quartet fraction	q	2/3	
hf transition $q \to d$	$\lambda_{qd}(\mu s^{-1})$	35(5)	37.0(4)
hf transition $q \to d$	$\lambda_{dq}(\mu s^{-1})$	[1)]	
ddμ form. rate from q	$\lambda_q(\mu s^{-1})$	~ 3.75	3.98(5)
ddμ form. rate from d	$\lambda_d(\mu s^{-1})$	2.549(23)	0.053(3)
effective fusion fraction	β	0.590(6)	0.517(15)
sticking probablity	$\overline{\omega}$ [2)]	0.1206(6)	
^{3}He total capture rate	$\Lambda_{He}(s^{-1})$	2216(70)	
^{3}He partial capture rate	$\Lambda_T(s^{-1})$	1496.0(40)	
μd quartet capture rate	$\Lambda_q(s^{-1})$	~ 10	
μd doublet capture rate	$\Lambda_d(s^{-1})$	~ 400	

Table 3: Kinetic parameters. All values given with error bars are directly determined experimentally, others theoretical. [1)] $\lambda_{dq} \sim \frac{q}{1-q} e^{-\frac{\Delta}{kT}}$, with the μd hyperfine splitting energy Δ=0.0485 eV and k=8.6174 10^{-5} eV/K (small deviations possible due to back-decay); [2)] it is convenient to define the effective sticking fraction $\omega = \beta\overline{\omega}$.

The vector $N(t)$ for the populations of the μd quartet, μd doublet, and μ^3He states

$$N(t) = \begin{pmatrix} N_q(t) \\ N_d(t) \\ N_{He}(t) \end{pmatrix} \tag{9}$$

with initial conditions

$$N(t=0) = \begin{pmatrix} q \\ 1-q \\ 0 \end{pmatrix} \tag{10}$$

obeys the following kinetic equation

$$\frac{dN(t)}{dt} = KN(t), \tag{11}$$

where

$$K = \begin{pmatrix} -\lambda_\mu^+ - \Lambda_q - \phi\lambda_{qd} - \phi\lambda_q(1-q(1-\omega)) & \phi\lambda_{dq} + \phi\lambda_d q(1-\omega) & 0 \\ \phi\lambda_{qd} + \phi\lambda_q(1-q)(1-\omega) & -\lambda_\mu^+ - \Lambda_d - \phi\lambda_{dq} - \phi\lambda_d(1-(1-q)(1-\omega)) & 0 \\ \phi\lambda_q\omega & \phi\lambda_d\omega & -\lambda_\mu^+ - \Lambda_{He} \end{pmatrix} \tag{12}$$

The observable time distributions include el(t) for the electrons, fus(t) for the ^{3}He fusion products, $cap_n(t)$ for the neutron from $\mu + d$ capture and $cap_T(t)$ for the tritons from μ+^{3}He capture.

$$el(t) \equiv \frac{dN_e}{dt} = \lambda_\mu^+ \sum_i N_i(t) \tag{13}$$

$$fus(t) \equiv \frac{dN_{He}}{dt} = \beta(\phi\lambda_q N_q(t) + \phi\lambda_d N_d(t)) \tag{14}$$

$$cap_n(t) \equiv \frac{dN_n}{dt} = 2(\Lambda_q N_q(t) + \Lambda_d N_d(t)) \tag{15}$$

$$cap_T(t) \equiv \frac{dN_T}{dt} = \Lambda_T N_3(t) \tag{16}$$

$$\tag{17}$$

5.3 Optimization of the Target Conditions

Fig. 8 shows time distributions calculated by numerically solving the full system of the linear differential equations (11). The goal of the experiment is the determination of the μd doublet capture rate, thus (i) the doublet population should be maximized (or at least well defined) and (ii) background from μ^3He minimized. To optimize (i), the density should be increased compared to the density ϕ=0.01 of the MuCap experiment. This accelerates the hyperfine transition according to the rate $\phi\lambda_{qd}$. Lower temperatures provide a significant advantage because the smaller rate λ_d leads to less quartet population (via recycling) and to less μ^3He production (ii). Moreover, at low temperatures the $dd\mu$ formation

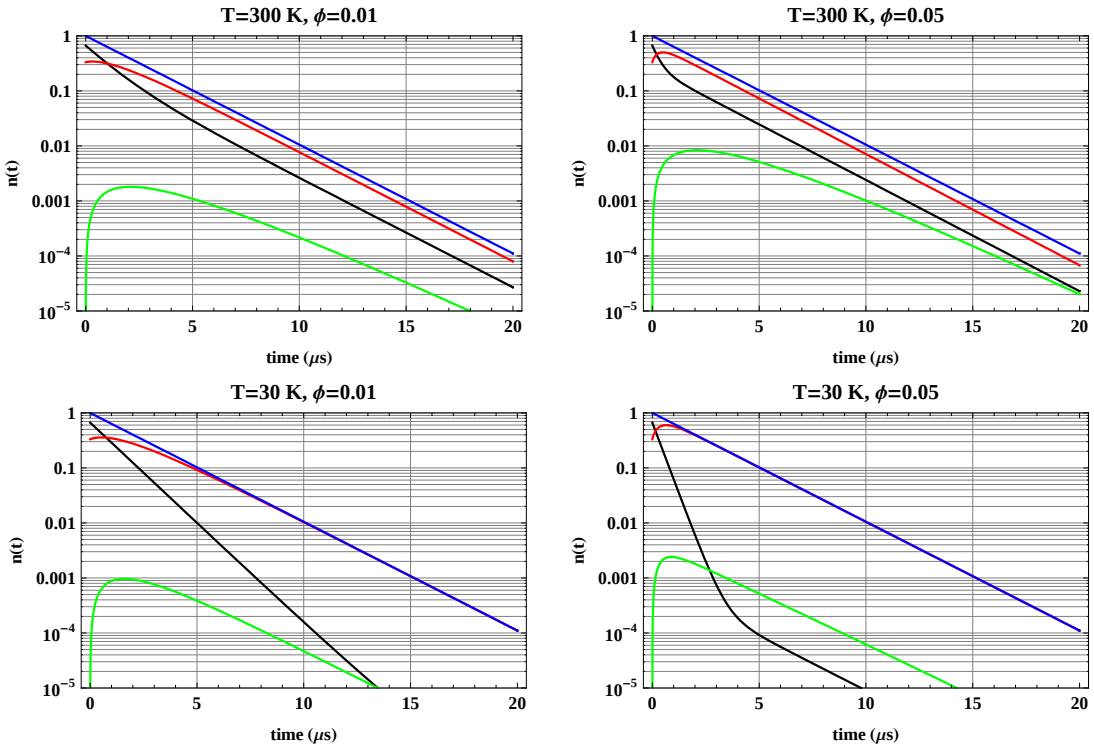

Figure 8: Time distributions of relevant states (blue=μd, red=$\mu d(\uparrow\downarrow)$, black=$\mu d(\uparrow\uparrow)$, green=$\mu^3$He) for different deuterium densities ϕ and temperatures T. The bottom right panel illustrates the optimized running conditions for the MuSun experiment.

rates λ_q and λ_d are dramatically different, making it easy to monitor the hyperfine populations via the fusion time distribution $fus(t)$. This fact is clearly demonstrated in Fig. 7, where the hyperfine transition rate is determined with high precision at low temperatures whereas the experimental uncertainty increases to 15% at T=300 K. Finally, T=30 K allows for 5 times higher density, while keeping the operating pressure comparable to the MuCap conditions, so that walls and entrance window thickness need not be increased. In summary, based on the physics requirements and practicability of the target design, the conditions ϕ=0.05 and T=30 K indicated in the right, lower panel of Fig. 8 were chosen as the baseline design of this experiment.

For a systematic study of the error contribution from all relevant quantities we used two methods, namely the first moment method and direct fits to Monte Carlo generated data sets. While we will describe the two studies in the following two subsections, it shall be noted that in both cases the set of investigated parameters was $\alpha = \{\lambda_q, \lambda_d, \lambda_{qd}, \Lambda_{He}, \omega\}$. An additional set $\alpha' = \{\lambda_\mu^+, \Lambda_q\}$ was studied for the fitting method, only. These parameters were then varied individually over a reasonable range in order to study their effects on the experimental observable of interest, i.e. the muon disappearance rate λ_μ^- (or equivalently the difference in appearance rates $\lambda_\mu^- - \lambda_\mu^+$). For this, we chose the experimental values from literature and allowed a $\pm 2\sigma$ variation with σ being the experimental uncertainty. This was compared to the variation of Λ_d by 1% as this corresponds to the best achievable precision for MuSun. The bottom line of both studies is that they are in line with each other and that the overall effect of the kinetic uncertainties in the various parameters is at a negligible level for the final determination of Λ_d to a precision of $< 1.5\,\%$.

5.3.1 First Moment Method

For this method we define

$$\delta\lambda \equiv \frac{\int_0^\infty N(t)dt}{\int_0^\infty t\,N(t)dt} - \lambda_\mu^+ \tag{18}$$

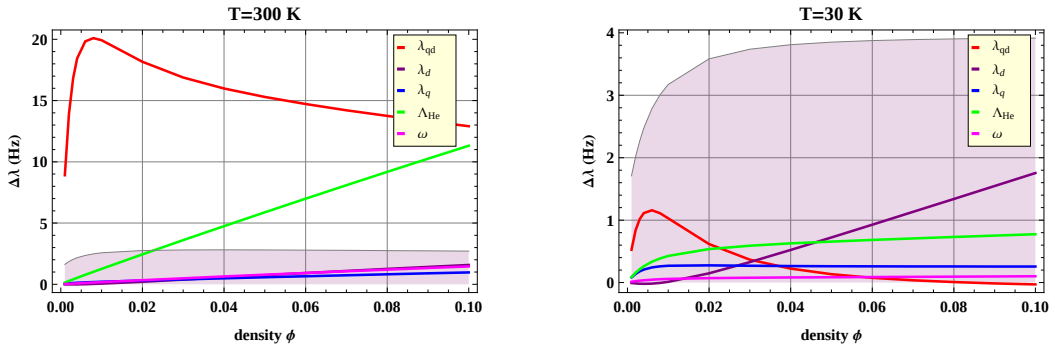

Figure 9: Effect of a 2σ variation of the kinetics parameters on the difference $\delta\lambda$ in the observed disappearance rates. The shaded area indicates the variation of $\delta\lambda$ for a variation of Λ_d by 1%.

where $\delta\lambda$ is an approximation for the difference in the disappearance rates $\lambda_\mu^- - \lambda_\mu^+$. In Fig. 9, the effect on the observable $\delta\lambda$ for changes of all parameters in the set α is shown as function of the density. In addition, the shaded area represents the effect of a fractional variation of Λ_d by 1% (i.e. the measurement goal). The left plot shows this study for T=300K and the right for T=30 K.

The density dependence is easy to understand. At the limit of $\phi \ll 0.01$ the μd hfs states remain in a nearly statistical mixture, therefore the dependence on λ_{qd} is reduced. However, the observed capture rate approaches the statistical rate $\approx \frac{\Lambda_d}{3}$ and therefore, the sensitivity to Λ_d decreases as well. At $\phi \gg 0.01$ the hyperfine transition becomes fast, nearly all μ atoms are in the doublet state and, as a consequence, the sensitivity to λ_{qd} is small again. Clearly, sufficient precision is difficult at 300 K, while the uncertainties are below 0.25% at 30 K and $\phi = 0.05$, thus at an almost negligible level.

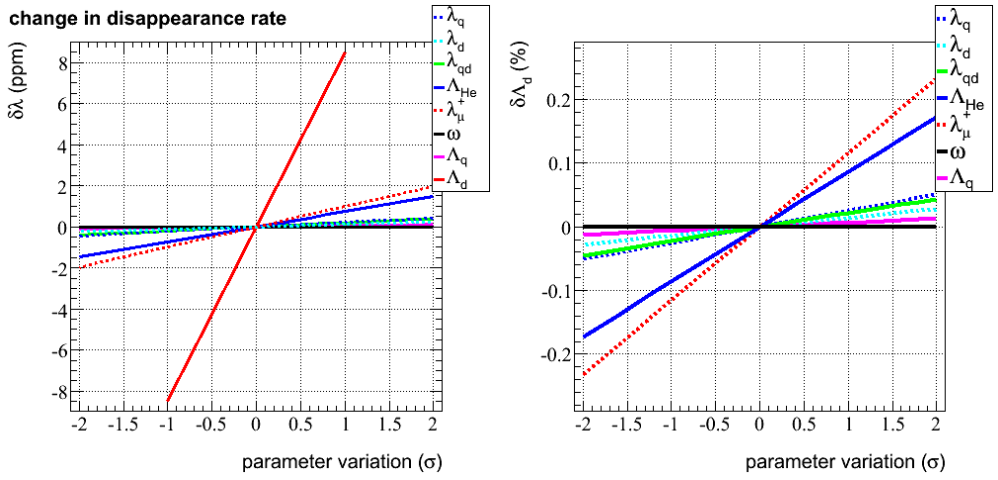

(a) (b)

Figure 10: (a) Sensitivity of the muon disappearance rate to the rate Λ_d and the set of kinetics parameters α and α'. (b) Fractional change in the "best fit" rate Λ_d due to variation of the parameters. The $\pm 2\sigma$ experimental uncertainties were: $\delta\lambda_\mathrm{q} = \pm 0.1 \times 10^6$ s^{-1} (blue dashed line), $\delta\lambda_\mathrm{d} = \pm 0.006 \times 10^6$ s^{-1} (cyan dashed line), $\delta\lambda_\mathrm{qd} = \pm 0.8 \times 10^6$ s^{-1} (green solid line), $\delta\Lambda_\mathrm{He} = \pm 140$ s^{-1} (blue solid line), $\delta\lambda_{\mu^+} = \pm 2$ ppm (red dashed line) and $\delta\omega = \pm 0.0037$ (black solid line). The rate Λ_d was varied by $\pm 1\%$ and the unmeasured rate Λ_q was varied by $\pm 20\%$ (magenta solid line).

5.3.2 Full Kinetic Fits

The impact of the experimental uncertainties in the kinetics parameters on the extraction of the rate Λ_d from the measurement of the electron time spectrum was also studied by a Monte-Carlo simulation

for the MuSun condition of T=30 K and $\phi = 0.05$. First, the analytical solutions obtained from the coupled differential equations describing the μd chemistry were used to generate electron time spectra. Next, the doublet rate Λ_d was extracted via a fit of the electron time spectrum to the aforementioned analytical solutions with all kinetics parameters fixed at the measured values. Last, by varying the values of the kinetics parameters when generating the electron time spectra, but fixing the values of the kinetics parameters when fitting the electron time spectra, the sensitivity of the rate Λ_d to the set of kinetics parameters α and α' could be determined.

As can be seen from the results shown in the Fig. 10, the sensitivity of the extracted rate Λ_d to the experimental uncertainties in the kinetics parameters (including correlations between kinetics parameters) is well below our best expected precision of $\pm 1\%$ in Λ_d. In addition, no significant sensitivity for variable fit start times in the range of 0 to 1 μs was found.

5.4 Observables

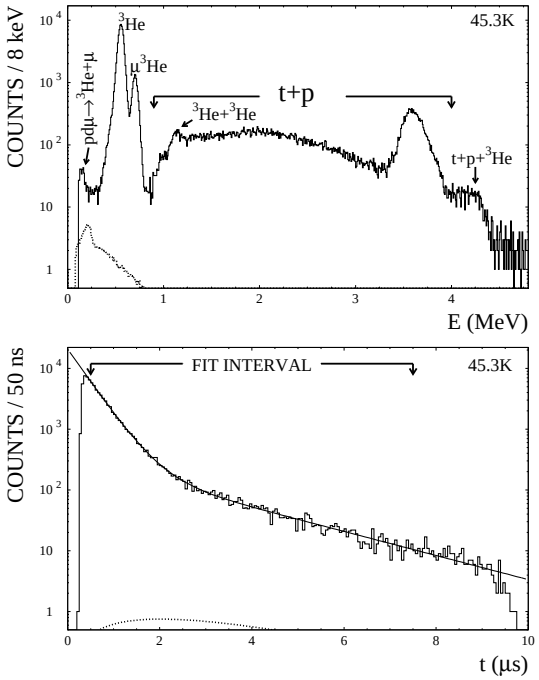

Figure 11: Charged particle spectra after muon stop from Ref. [56]. The conditions were T=45.3 K (which is very close to the operating point of MuSun), ϕ=0.0524 and nitrogen impurity level $c_N \approx 41$ ppb. Impurity capture background indicated by dotted line.

The primary observables for the precision measurement of the muon decay rate are the muon track in the TPC and the decay electron vector reconstructed by the electron tracker. In addition, critical information for the unambiguous interpretation of the experiment is derived from the detection of charged particles from fusion and impurity capture within the TPC and with external neutron and gamma detectors. Table 4 and Fig. 11 show the properties of these charged particles in the TPC as observed under similar conditions in a previous experiment [56]. The events below 3.6 MeV are due to proton tracks escaping the sensitive volume. Two small peaks at 1.2 MeV and 4.2 MeV indicate the pile up of two subsequent fusion signals within 200 ns for ^{3}He+^{3}He and $(t+p)$+^{3}He, respectively. Events below 0.45 MeV are due to pd fusion and gas impurities. Complementary information on fusion and capture neutrons is provided by neutron detectors, which have small efficiency, but provide excellent time resolution.

	E (MeV)	E_{obs} (MeV)	R(mm)
^{3}He	0.82	0.6	0.18
μ^3He	0.80	0.75	0.6
t	1.01		1
p	3.02		16

Table 4: Recoil energies and range of fusion products at ϕ=0.05. The observed energies are lower due to charge recombination.

6 Experimental Setup

6.1 Cryogenic Time Projection Chamber

6.1.1 Main Design Considerations

The baseline design of the cryogenic TPC is presented in Fig. 12. We define the chamber coordinate system with the x-axis horizontal and transverse to the beam direction, the y-axis pointing vertical up and the z-axis along the beam direction. At the gas density ϕ=0.05 it will operate without gas amplification as a cryogenic time-projection chamber (cryo-TPC). The main design criteria are as follows.

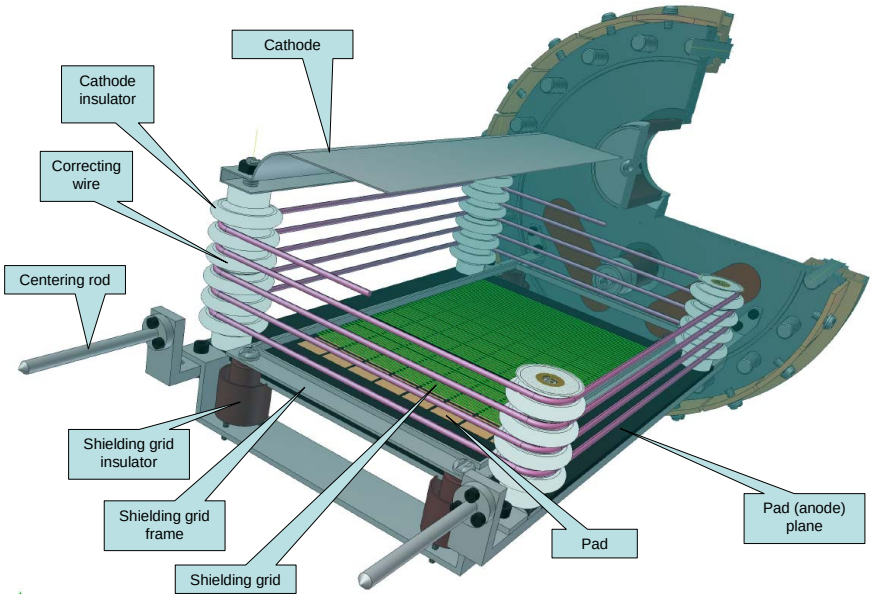

Figure 12: Cryo-TPC layout with the main components described by the labels.

The size of the sensitive pad area is determined by the properties of the πE3 muon beam and the scattering in the beryllium entrance window. GEANT Monte Carlo simulations, tuned to the observed MuCap stopping distributions, predict that 85 % of incoming muons will stop over a horizontal 100×100 mm^2 pad area (along the z (beam) and x (transverse to beam) axis). The chamber height of 80-100 mm (vertical axis y) was chosen to contain most of the beam. This choice is critical, as it determines the required drift high voltage U_d. With U_d=100 kV, the electric field to pressure ratio is E/P=0.2 kV/cm-atm (same as for MuCap). According to Fig. 13 this results in an acceptable recombination R_α = 0.82 and a drift velocity $v_d \approx 0.4$ cm/μs. Gas gain is difficult to achieve as the field on the anode wires' surfaces would need to be increased by about 5 times due to the higher gas density compared to the MuCap conditions. However, intrinsically an ionization chamber is more robust and capable of higher resolution than a proportional chamber. Therefore, gas amplification is not necessary if an overall resolution of 30-50 keV can be achieved in the pad readout.

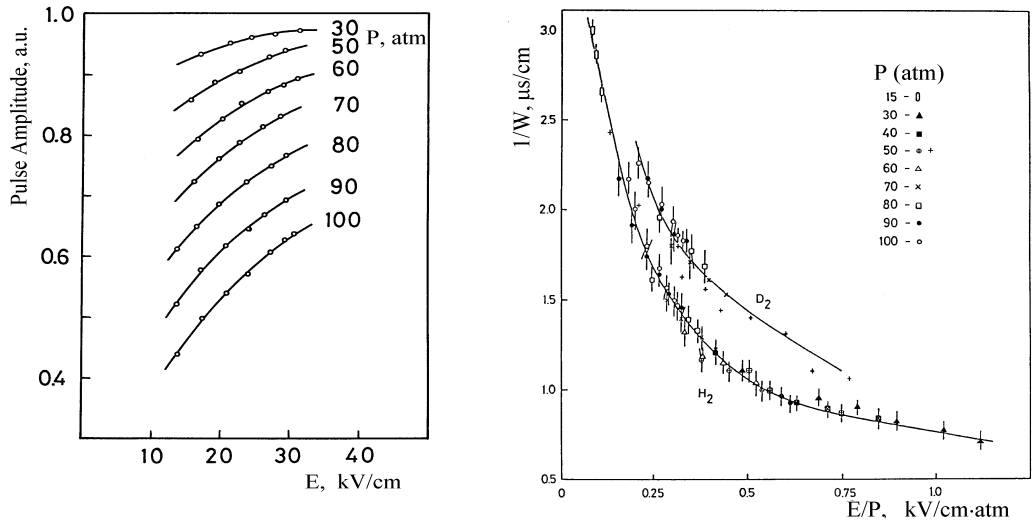

Figure 13: Recombination and drift velocity from Ref. [56]. The MuSun conditions correspond to P=50 atm, E=10 kV/cm and E/P= 0.2 kV/cm-atm.

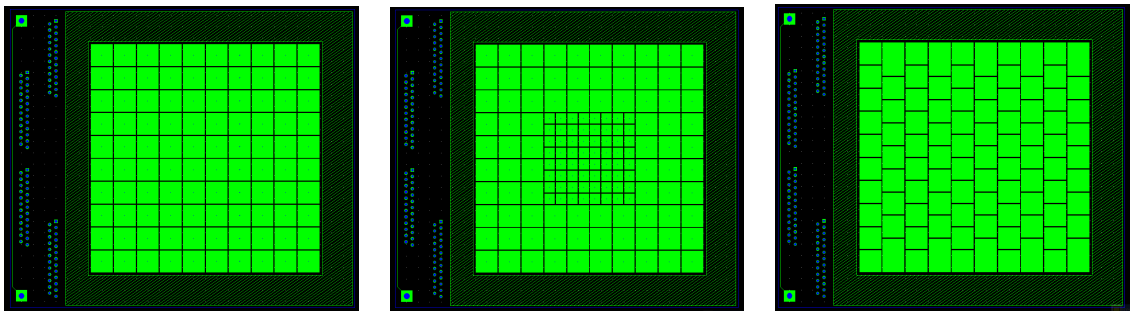

Figure 14: Pad layout variants under consideration. Left: Baseline 10×10 mm^2, Center: 5×5 mm^2 in center, Right: "Brick wall" for improved x tracking

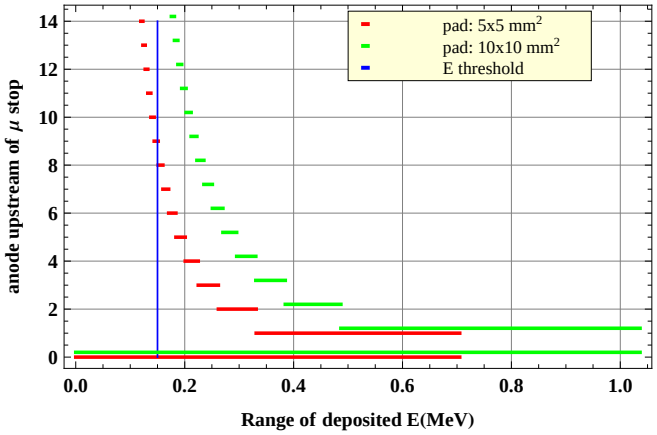

Figure 15: Muon energy deposition on anode pads. The anode number 0 corrsponds to the muon stopping pad, whereas the higher anode number are the pads upstream of this muon stop position along the incoming muon path.

For the baseline configuration we divide the readout plane into 100 pads of each 10×10 mm^2 in size. An R&D program including Monte Carlo studies as well as experiments with prototypes is foreseen to define the final optimized layout. Some choices currently considered are indicated in Fig. 14. A total number of 100-200 pads would be well matched to our existing custom made FADCs and the DAQ for full analog readout. During this R&D studies, the following requirements need to be optimized:

- The muon energy deposition relative to the stopping pad is shown in Fig. 15. With 10×10 mm^2 pads, all muons entering the chamber deposit enough energy per pad so that they are detected above threshold along their entire path. In comparison, a 5×5 mm^2 pad size would give higher spatial resolution, but the muons are only detected up to ≈ 35 mm upstream of the pad where the muon stops. Both pad sizes are acceptable for imposing muon - decay electron vertex cuts to suppress background, as this impact cut will not be tighter than 10 mm to avoid time-dependent effects from μd diffusion.

- The energy resolution will deteriorate with the square root of the number of pads accumulating the signal, as it is dominated by the readout cable capacitance and preamplifier noise. For ^{3}He fusion recoils with a range of 0.18 mm, about twice as many fusion recoils will escape a pad for 5 mm compared to 10 mm pad length. In both cases, the effect is at the percent level only.

- Impurity detection might be the strongest argument for higher granularity in at least part of the pad plane. As discussed below the detection of proton emission after muon capture on trace levels of nitrogen contaminants might provide a definitive signature to distinguish impurity capture from the frequent ^{3}He+n fusion channel.

- The systematic effects due to muon fusion overlaps would be reduced by higher granularity. As this effect leads to systematic distortions of the time spectrum, it should be minimized by an optimal detector geometry.

6.1.2 Technical Design

The cryo-TPC is filled with ultrapure deuterium and works at low temperatures T$= 25 - 35$ K and densities of $\phi = 0.05 - 0.08$ relative to liquid hydrogen density. According to the thermodynamic properties of gaseous deuterium in Fig. 16 this corresponds to a pressure range of P$= 4 - 6.5$ bar. Fig. 12 shows the main parts of the chamber and it specifications are given in table 5.

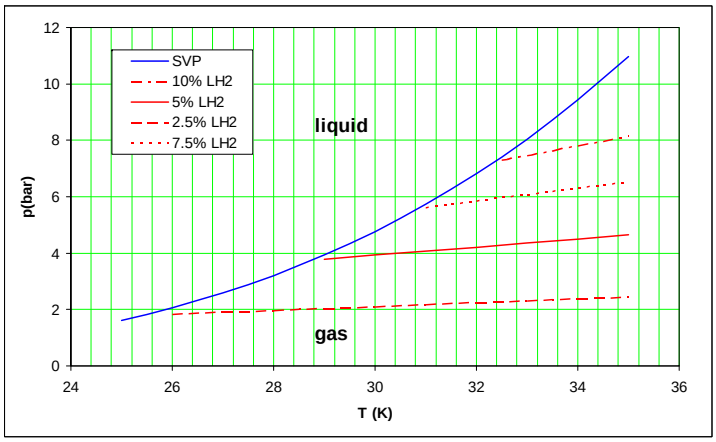

Figure 16: Saturated vapor pressure curve and isochores for cryogenic deuterium.

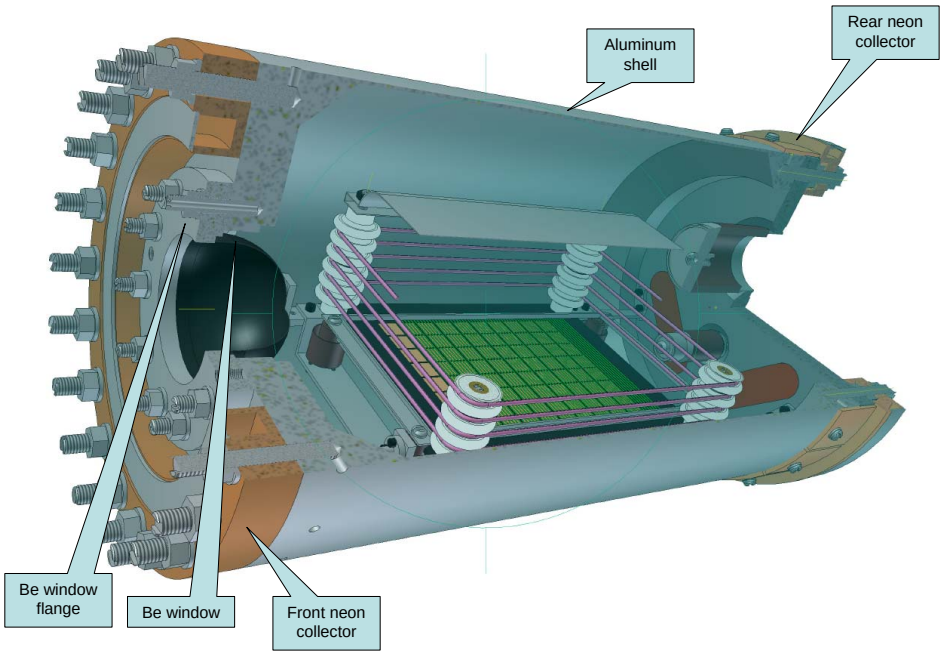

Figure 17: Cryo-TPC with pressure vessel.

system	parameter	value
Drift cathode	potential U_d	-80 to -100 kV
	cathode-grid distance	80 mm
Grid	potential U_g	-3 to -5 kV
	grid-anode distance	1 mm
	wire pitch	400 μm
	wire diameter	55 μm
	wire material	stainless steel
Anode	area	100×100 mm^2
	pad size	10×10 mm^2
	total number pads	100
Performance	drift velocity	0.4 cm/μs
	drift time cathode to grid	25 μs
	drift time grid to anode	$\approx$ 150 ns
	energy resolution	30-50 keV
	energy threshold	150-200 keV

Table 5: Cryo-TPC specifications

At the top of the chamber is the high voltage cathode. Its tent-like shape helps to establish a constant electrical field between the cathode and the first field shaping wire. The final spacing and geometry of the field shaping wires will be determined using standard electric field calculation software in order to obtain a homogeneous field distribution in the drift region. The drift volume is separated by a (Frisch) grid from the detection pad plane. The grid is mounted on 4 ceramic insulators with possibility to vary distance between the anode pad plane and the grid from 0.5 mm to 1.5 mm. For the moment, we foresee a distance of 1 mm still being subject to further optimization. The anode pad plane is fixed on a supporting frame with centering pins on the front end. These will be connected to the front flange of the aluminum shell to protect the cryo-TPC against vibrations.

The grid consists of the frame and the wires which are soldered on the long side of the frame (wires along x direction). It works as an electrical screen for the positive charge in the cryo-TPC and is transparent for the electrons drifting from the cathode to the anode plane. The grid wires will have a diameter of 55 μm, a pitch of 400 μm and will be strung with a tension of 60 g. For a total number of 325 wires this adds to a total distributed load of 19.5 kg. The internal stress distribution and deformation of the frame was calculated with the finite element code ANSYS. The calculated values of deformations guarantee that at all temperatures the wires sagging will be less then 80 μm, corresponding to 8% of the 1 mm distance between pad plane and grid, which is below the homogeneity requirement for the electrical field.

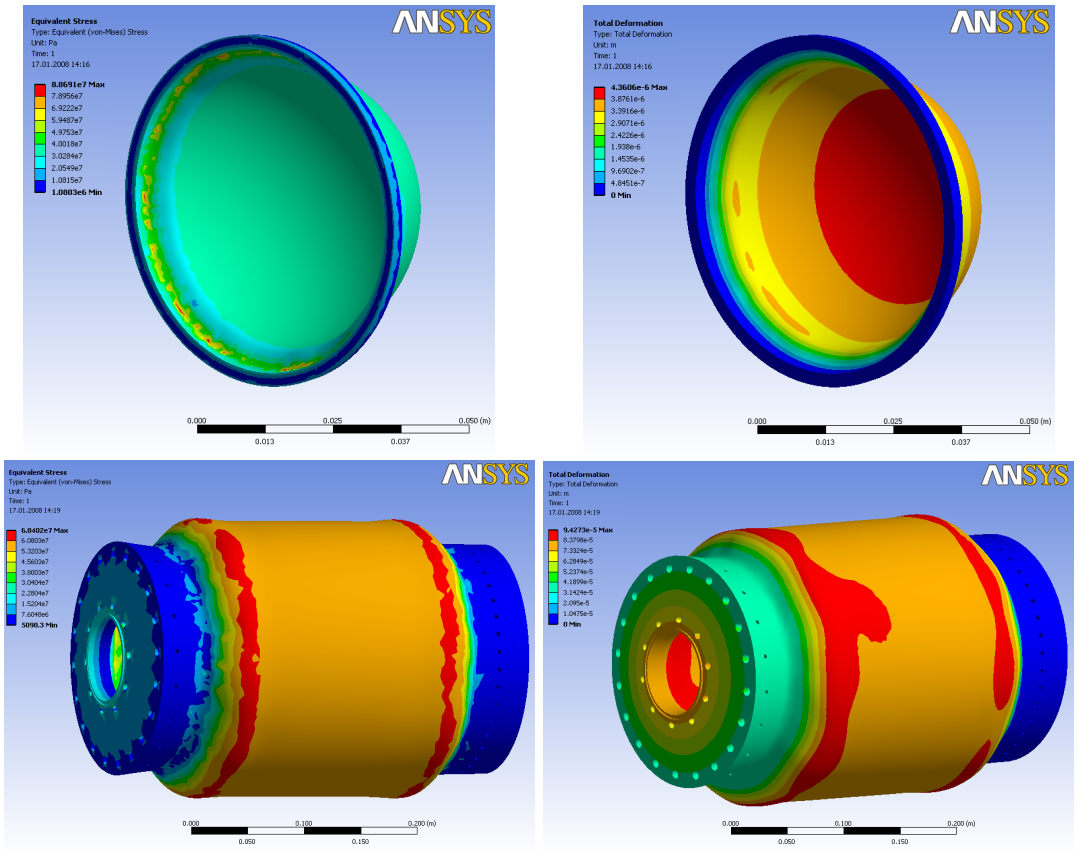

Figure 18: ANSYS calculations of the stress (left plots) and the deformation (right plots) for the window and the entire pressure vessel. The maximum scale (red areas) for the stress and deformation are: 88.7 MPa and 0.005 mm for the window and 68.4 MPa and 0.1 mm for the entire vessel.

Onto the rear flange (Fig. 17) of the cryo-TPC vessel several ceramic feedthroughs are welded: The 100 kV feed-through for the cathode, the 10 kV feed-through for the grid, and two 50-pin signal connectors for the signals from the cathode pad plane. The cryo-TPC active target is placed inside an aluminum shell which has to be thin to transmit the decay electrons, but thick enough to provide the necessary strength against the pressure in the chamber. ANSYS calculations (Fig. 18) indicate that this can be achieved with a side wall thickness of 2.5 mm leading to a maximum stress of 68 MPa.

Different aluminum alloys give different numbers from 150-300 MPa. We have about 2-3 times reserve of the aluminum shell strength. The spherical beryllium window for the input muons and two neon collectors for the cooling of the target will be installed on the front flange. The window is a beryllium semi-sphere welded into the stainless steel flange and it has a diameter of 61 mm and a thickness 0.4 mm. Calculations of the stress distribution and deformation distribution are shown in Fig. 18. All calculations were done at a pressure of 10 bar and room temperature. The maximum stress is 88.7 MPa. The hot-pressed beryllium maximum stress value is 200-300 MPa, so that there is a reserve of about 2-3 times in the stability of the window. We are planning to carry out a number of tests to evaluate the window performance at cryogenic temperatures. The mechanical properties of the system of the stainless steel flange and the beryllium window at low temperatures are improved, but we have to evaluate the thermal stress. For the connection of the beryllium window to the chamber and the rear flange we are using cog-groove type compaction with an indium wire in between. This type of connection is well known for cryogenic applications and suitable for our pressures. The choice of the Al alloy and the overall design will be finalized in accordance to the PSI/Swiss safety requirements and procedures.

6.2 Cryogenics and Gas System

For the cooling system of the cryo-TPC (see Fig. 19), we are planning to use the cold head COOLPOWER 140T by Leybold. At 25-35 K, the cold head can produce about 30 W cooling power, which is sufficient. We propose to use a heat pipe system with neon. From the cold head's lower flange the cooling power is transported through flexible copper elements (to suppress the transmission of vibrations) to the neon condenser where the neon gas is liquified. Running down a vertical tube, the liquid neon is collected in two heat exchangers that are mounted on both ends of the chamber with good thermal contact to the body of the chamber. Each heat exchanger is equipped with a heater (for precise temperature stabilization) and a temperature sensor (Pt500 or Pt1000). Additional heater and temperature sensors on the neon condenser enable to control the necessary level of liquid neon in the vertical tube. The liquid neon vaporizes in the heat exchangers and returns to the condenser. To exclude any transmission of vibration from the cold head via vacuum insulation, the vacuum flange of the cold head is connected to the vacuum chamber via a bellow with a vibration-free support.

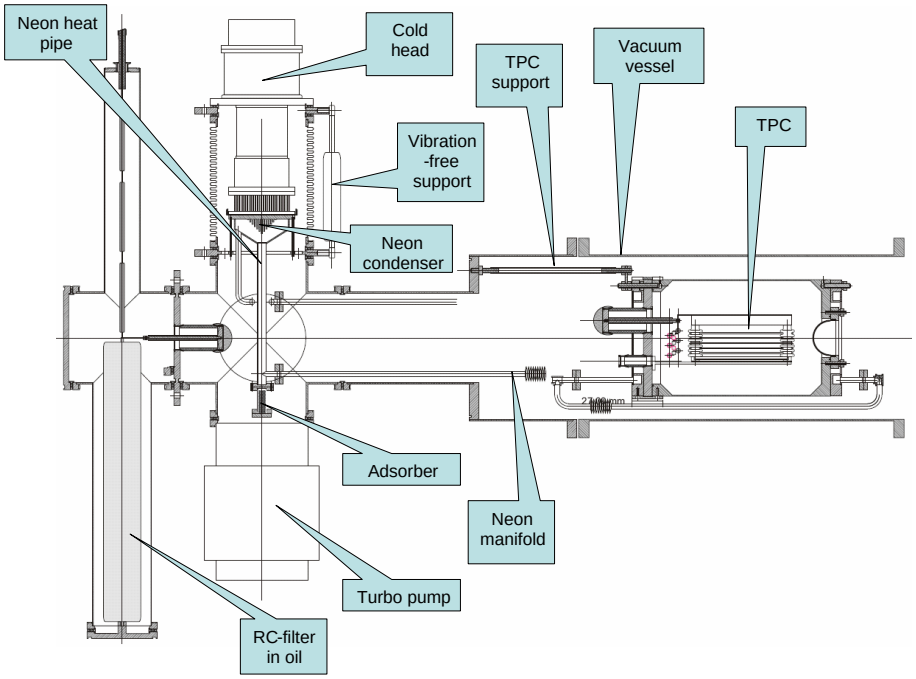

Figure 19: Overall cryogenic system as described in the text.

6.2.1 Chemical Purity

It is impossible to provide the required ultra-high chemical purity of deuterium only by means of initial purification. Various contaminants (especially air components and moisture) will migrate to the gas from chamber elements and sealings even under cryogenic conditions. The existing circulating cryogenic system for continuous ultra-high hydrogen purification [59] from MuCap will be used for the removal of contaminants in the deuterium gas. This system was successfully used to provide ultra-high purity of deuterium-depleted hydrogen in the MuCap experiment and an excellent purification power during several MuCap runs between 2004-2007 was achieved. The quality of the purification was monitored by gas chromatography and by means of an online humidity sensor. The achieved results [59] corresponded to MuCap demands (7 ± 1 ppb of N_2; < 5 ppb of O_2, $\approx$10 ppb of H_2O). The system consists of three base units: compressor, purifier and automated control system. The compressor has to provide a constant flow of hydrogen through the purifier with a rate high enough to support the specified purity of the gas in the TPC. Since the compressor works as a cryopump it has the following advantages: big reliability, and a large range of gas flow rate. A cryopump is based on the ability of a special substance (adsorbent) to absorb considerable amounts of gas while cooled and relieve them upon subsequent heating. In our case, activated carbon is used as the adsorbent and its cooling and heating are provided by liquid nitrogen and electrical heaters, respectively.

The principle of operation of the purifier is based on prevalent (in comparison with the main component, hydrogen) adsorption of contaminations (nitrogen, oxygen, water etc.) in an adsorption filter. Synthetic zeolite is used as the adsorbent for this goal. To increase the rate of purification, the filter is strongly cooled with liquid nitrogen (the same as for the cryopump). The adsorption method of purification guarantees a high level of purification at the very wide range of species. The automated control system consists of a microprocessor control block, a set of sensors and devices (remotely controlled valves, mass-flow controllers and heaters), and a control PC. This control unit organizes the operation of the system in fully automatic mode. It provides all sensor interfaces and low-level control procedures. The advantage of the system is the ability to provide relative pressure stability at the level of better than 0.1%. The system is designed following all hydrogen safety precautions and it protects the detector from overpressure damage in case of vacuum problems. This general-purpose cryogenic adsorption method allows using the system for cleaning of deuterium as well as protium without major changes.

The cryopump can support circulation of deuterium at the same level as protium and the same contaminants (O_2, N_2, water) are removed. To provide the final extra-cleaning, an additional adsorption filter will be introduced in the new cryogenic scheme. This filter is mainly identical to the filters of the purifier but it is cooled by liquid neon. Its temperature corresponds (or even slightly lower) to the temperature of the detector ($\approx$30 K) which is about 37 degrees lower than the temperature of the filters of the purifier. This temperature difference provides sufficiently better cleaning conditions on the final stage of purification.

6.2.2 Isotopic Purity

The cryogenic separation facility (Deuterium Separation Unit, Fig. 20) will be used to provide a good initial isotopic purity. This setup was designed and built in 2006 for MuCap. Based on the achieved results with H/D mixtures, we expect to be able to produce pure deuterium with less than 1 ppm protium contamination. We briefly review the system as used.

The facility uses the well-known rectification method to separate isotopes of hydrogen using the difference in saturation vapor pressure of separating species above the surface of a liquid mixture. It can be considered as a multi-step distillation with the use of a column filled with special material (either a set of perforated plates or a particular packing) to increase a phase contact surface. A condenser is placed on the top of the column to liquify the vapor mixture. This liquid, called reflux, then returns into the top of the column. The vapor can also be partially taken away from the top of the column as a pure product of the process. The reflux drains down along the column, moistening the packing. An amount of the liquid suspended on the packing is a column holdup. The lower end of the column is equipped with a reboiler. A separated mixture boils in the reboiler forming the vapor, which rises upward along the column and interacts with the counter flow of draining reflux. The liquid is saturated with the high-boiling component, and the gas with the low-boiling one. For the hydrogen isotopic separation the cryogenic modification of the rectification method is used. A separation column of 2.2

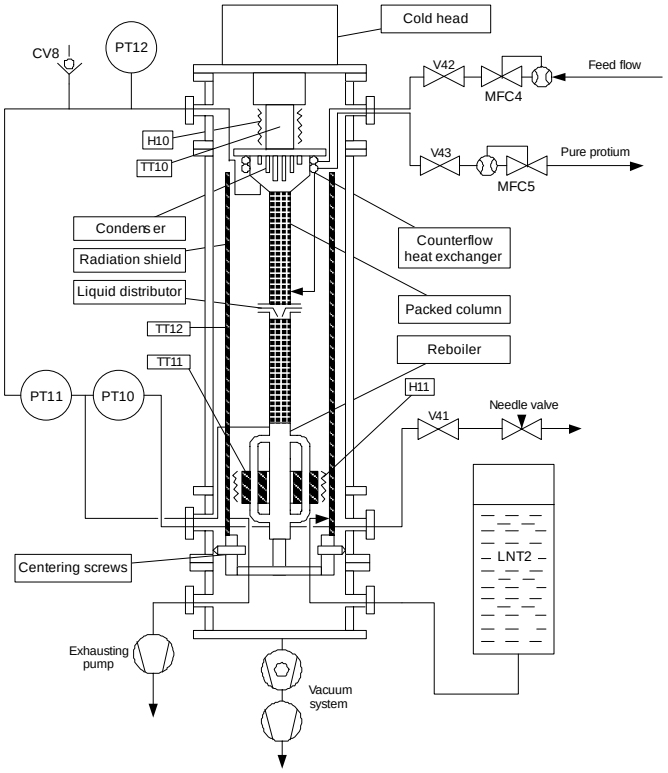

Figure 20: The isotope separation system. The main components are the cold head with the condensor at the top, the packed column where the actual separation takes place, and the reboiler at the bottom.

cm inner diameter and 155 cm overall packing height is cased into a vacuum heat insulation volume. Liquification of the distillated gas is provided by the 20 W cold head connected to the condenser. The specially designed control system provides the necessary algorithms for the column operation. The schematic drawing of the separation unit is shown in Fig. 20. As a result of the column operation using natural hydrogen as the source gas, H_2 with a concentration of HD molecules less than 6 ppb was obtained; that is the most isotopically clean protium in the world. The result was confirmed by direct measurements with a large compact accelerator at the Institute of Particle Physics, ETH-Zurich, Switzerland [60].

6.3 Detectors

Whereas the essential detector, the cryo-TPC, was described in a separate section 6.1, we will now review the other relevant components, their role with respect to the measurement and the design criteria. Most of these components come from the existing MuCap experiment, while some additional detectors will be added for MuSun. A schematic view of parts of the full system was shown in Fig. 5.

6.3.1 Entrance Detectors

Entrance muon detectors provide timing of incident beam muons and enable the selection of events where only one muon entered the target ("pileup protection"). These detectors are thin to avoid degrading the beam, which would adversely affect the spatial stopping distribution of muons within the hydrogen gas. The elements between the beam window and the entrance window of the pressure vessel containing the D_2 are described below in the order encountered by a beam particle.

The first detector is a 500-μm-thick muon scintillator, the μSC, to provide a fast timing signal.

Parameter	ePC1	ePC2
Number of anode wires	512	1024
Number of inner cathode strips	192	320
Number of outer cathode strips	192	320
Operating voltage	+2.6 kV	+2.8 kV
Half-gap	4 mm	4 mm
Diameter at anodes	384 mm	640 mm
Active length	580 mm	800 mm
Anode spacing	2.356 mm	1.963 mm
Inner cathode screw angle	43.81 deg.	44.31 deg.
Outer cathode screw angle	46.19 deg.	45.74 deg.

Table 6: Physical parameters of the electron proportional chambers (ePCs).

After the μSC is the μSCA, a scintillator with a 35-mm-diameter hole in the middle to allow most beam particles to pass. Its purpose is to veto muons that are too far off the beam axis. Immediately behind the μSCA and aligned to it is a lead collimator also with a 35-mm-diameter hole.

A multiwire proportional chamber, the μPC, follows the lead collimator. The μPC has two anode planes, each with 24 wires, and 25-μm-thick aluminized mylar cathode planes. The anode planes are oriented such that one provides horizontal (x) positions of beam particles, and the other provides vertical (y) positions. The μPC improves the pileup-protection efficiency compared to the μSC alone.

We are considering to place a thin double sided silicon strip detector inside the insulation vacuum to facilitate the beam targeting onto the Be window into the D_2 pressure vessel.

6.3.2 Electron Detectors

MuSun will use the MuCap electron tracker which consists of two cylindrical chambers (ePC1, ePC2) and a scintillator hodoscope (eSC).

The electron tracking detectors are two concentric, cylindrical multiwire proportional chambers, each with readout of anodes and cathode strips, to give the complete (ϕ, z) positions (in cylindrical coordinates) of an electron track at two different radii. The smaller chamber (ePC1) sits just outside the pressure vessel. The larger chamber (ePC2), with about twice the diameter as the smaller one, sits somewhat inside the scintillator hodoscope barrel (eSC). Anode wires run parallel to the cylinder axis, and cathode strips wrap around the chamber making an angle of ≈ 45 degrees with the anodes. The inner and outer cathode planes wind in opposite directions, providing redundancy if the anode and both cathode planes of a chamber are required. Physical parameters of ePC1 and ePC2 are given in Table 6.

The anode and cathode planes are fully instrumented with chamber-mounted, charge-integrating-preamp-discriminator cards. Although mounting the preamps directly on the chambers reduced electronic noise into the sensitive preamplifiers, it was necessary to shield the cards and the entire chamber from external electromagnetic interference via thin copper meshes. The outputs of the preamp/discriminator cards are connected to custom data acquisition modules through 40-wire twisted pair cables (32 wires are used for signals, the remaining for threshold setting and preamp power), and each cable is wrapped in braided wire shielding. The custom data-acquisition modules, called compressors, are based on FPGA circuitry. The discriminated signals from the ePC electronics are transmitted as low-voltage differential signals (LVDS) to the compressors, which encode them into time–channel words that are saved in a buffer.

Fast timing of electrons is the purpose of the eSC, a scintillator hodoscope comprising sixteen segments, each with an active area of 90×15 cm^2 placed with the long axis parallel to the beam axis, together forming a barrel with a diameter of 78 cm. Each eSC segment has two 5-mm-thick scintillating plastic layers with photomultiplier tubes on both ends. The total of 64 photomultiplier signals are input via discriminators to data acquisition modules (CAEN V767 time-to-digital converters) that record the time of each leading edge with 1.25 ns precision. In addition, the full analog signals are read out by custom built 8-bit wave form digitizer (WFD) boards. The time difference between detection by the upstream and downstream photomultipliers provides some information about where the particle hit along the length of the segment. All four photomultipliers on a given segment are required to be

in coincidence in the data analysis. The 4-fold coincidence reduces the level of random noise from the eSC as well as afterpulsing, generally leaving only signals from real particles.

6.3.3 Neutron Detectors

Muon stops in deuterium yield two distinct sources of neutrons: (i) fusion neutrons following $d\mu d$ molecule formation and the subsequent μ-catalyzed $d + d \rightarrow {}^3\mathrm{He}{+}n$ fusion reaction, and (ii) capture neutrons following the $\mu + d \rightarrow n + n + \nu$ capture reaction from the two μd atomic spin states (F=$\frac{1}{2}$, $\frac{3}{2}$). The $d\mu d$ fusion neutrons are monoenergetic with a kinetic energy of 2.45 MeV. The μd capture neutrons—although peaked at energies of 1-3 MeV—include an energetic component that reaches 53 MeV. The time dependence of the fusion neutrons and capture neutrons are shown in Fig. 21. Additionally, neutrons are emitted following muon capture on impurity atoms such as nitrogen, and coincident detection of capture recoil and capture neutrons may assist in separating these rare 'impurity' events from the large fusion background.

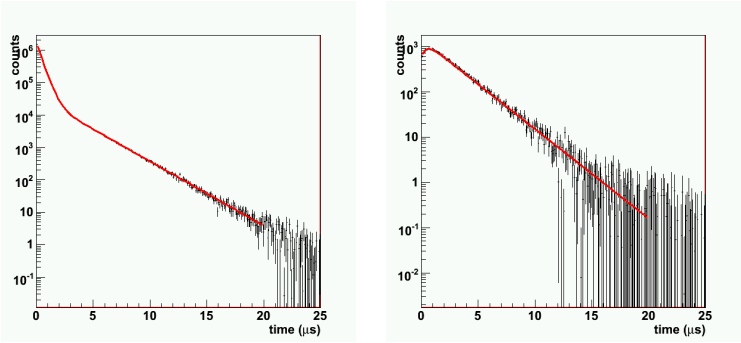

Figure 21: Simulated time distribution of fusion neeutrons (left) and capture neutrons (right) for $T = 30$ K and $\phi = 0.05$. Also shown are the results of the fits to the neutrons time spectra from the solution of the μ^-d kinetics equations.

We consider two possible configurations for neutron detection: (i) a "dedicated" neutron counter setup with neutron counters situated immediately outside the TPC vessel, and (ii) a "parasitic" neutron counter setup with neutron counters situated outside the eSC array similar to the one already used in the MuCap run. The parasitic neutron setup would record neutrons from the full sample of several 10^{10} muon stops in deuterium, whereas the dedicated neutron setup would record neutrons from a subset of 10^9 muon stops in deuterium. As a benchmark design for this setup we assume the use of 8 DEMON neutron counters in an identical configuration as used for MuCap. These detectors comprise cells of NE213 organic scintillator coupled to 13 cm diameter XP4512B photomultipliers. Each cell is 16 cm in diameter, 20 cm in length and contains 4 liters of liquid scinitillator. Each cell has a 6.35 mm thick Al entrance window and a 21.5 mm thick cylindical walls. The detectors are read out with custom built 12-bit FADCs, which allow offline reconstruction and optimization of their neutron - gamma separation.

6.3.4 Gamma Detectors

Auxilary gamma detector are considered for tagging the capture events on impurities. We discuss them briefly in section 7.2 on systematics.

6.3.5 Electronics and Data Acquisition

The data acquisition (DAQ) system will provide the read out, event building and data storage for the entrance muon detectors, outgoing electron detectors, cyrogenic TPC, neutron detectors and various slow control items such as the HV systems, beamline system, etc. An online analysis layer will enable both monitoring and diagnostics of the incoming data.

A substantial amount of acquisition infrastructure will be inherited from the existing MuCap experiment. Specifically, the readout apparatus for the electron detector will be carried forward, while

we propose upgraded electronics for the new TPC. The system provides for the untriggered readout of data blocks during the livetime of the DAQ, each typically ∼0.1 s, from many different types of electronics. It has been demonstrated to function with total data flow rates up to ∼15 MB/s with livetime fractions of 80% or better. The software is based on the MIDAS framework developed at PSI and TRIUMF, and it includes both online compression and real-time analysis.

Details of the various components of the acquisition system are given below:

- Electron readout system

  Data from the electron detector scintillators are recorded in two parallel data streams. Leading edge discriminators are used to produce digital signals, and these hit times are recorded by a CAEN V767 time-to-digital converter (TDC). This VME module has 128 channels; with an external clock speed of 25 MHz, it provides 1.25 ns time resolution. In addition, a set of 500 MHz waveform digitizers (WFD), originally developed by the Boston University group for the MuLan/MuCap experiments, will be used to record all of the pulse shapes from the electron scintilators. Only the CAEN TDC data were available for the first published result, but a comparison with the WFD is underway as part of the full analysis effort.

  Electron proportional chamber hits are digitized with a system of custom multichannel time-to-digital converters. Named "COMET", these devices have a time resolution of 20 ns and are able to compress clusters of simultaneous hits in nearby wires into a single data word. While these boards are housed in VME crates, they do not transfer data via the standard VME protocol; rather, they send it into the acquisition system through a Struck SIS3600 latch module.

- TPC readout system

  A new acquisition sub-system will be implemented for the cryogenic TPC. It will provide for the digitization and the readout of all pulses on all pads of the TPC. The distribution of hits in space and time will enable the three dimensional tracking of both incoming muons and charged products (e.g. protons, deuterons, etc) from impurity capture. Additionally, the pulse-shape digitization will enable particle identification based on energy loss, and be important for the discrimination between muon stops, fusion events and capture events.

  The baseline design for the cryogenic TPC is a 10×10 array of anode pads. Each pad will be readout via a custom pulse splitter card to two 8-bit waveform digitizer channels (the BU waveform digitizers that were developed for the MuLan experiment). The combination of low gain output and a high gain output from the splitter cards will provide the required energy resolution and dynamic range for both low amplitude and high amplitude pulses. The digitizers will operate at approximately 50 MHz to enable sufficient spatial resolution in the TPC drift direction.[4]

  The setup will utilize a total of 200 digitizer channels, or 50 digitizer modules. The digitizers will be distributed over four VME crates and readout by four rack-mounted frontend processors. The data will be transferred from the FIFO memories of the waveform digitizer channels to the random access memories of the frontend processors via Struck SIS3100/1100 bridges.

  For the estimation of the data rate from the cryo-TPC we have assumed an incoming muon rate of 30 kHz, an average of 10 pads per incoming muon, a total of 24 ADC samples per pad hit, and an average of 2.5 bytes per ADC sample. This yields a data rate of about 15 MB/sec in total and about 4 MB/sec per VME crate. Lossless compression of the incoming data-stream is expected to reduce this data volume by one third or better.

- Other readout systems

  Two additional CAEN TDCs are used to record signals from the muon entrance counters and other miscellaneous sources. Finally, the DEMON neutron detectors are read out by custom 12-bit, 170 MHz WFDs.

A total of eleven front-end crates contribute data to be stored. Four of these contain single-board VME computers, while six (those holding the BU waveform digitizers that will instrument the TPC

[4]Most likely the digitizers will be operated at a higher clock frequency with either firmware ADC summation or software ADC summation yielding an effective 20 MHz rate.

and eSC) have dedicated PCs connected through Struck SIS1100/3100 VME interfaces; the 12-bit WFDs interface directly to Ethernet. Their operations are coordinated by MIDAS remote procedure calls passed over the gigabit Ethernet network that interconnects them. Corresponding blocks of data from all of these sources are merged together by an event-builder process running on a dual-processor PC, which also applies lossless compression techniques. It then records a copy on a local tape drive and also transfers a copy to PSI's central archive system. An online analysis layer – receiving a fraction of events – will be used for integrity checking and online histogramming.

6.4 Monte Carlo Simulation

We have developed a GEANT-based Monte Carlo program in order to simulate the MuSun setup. A sketch of the setup as it is generated by the simulation program together with a typical μ-e decay event is shown in Fig. 22 for different views of the setup.

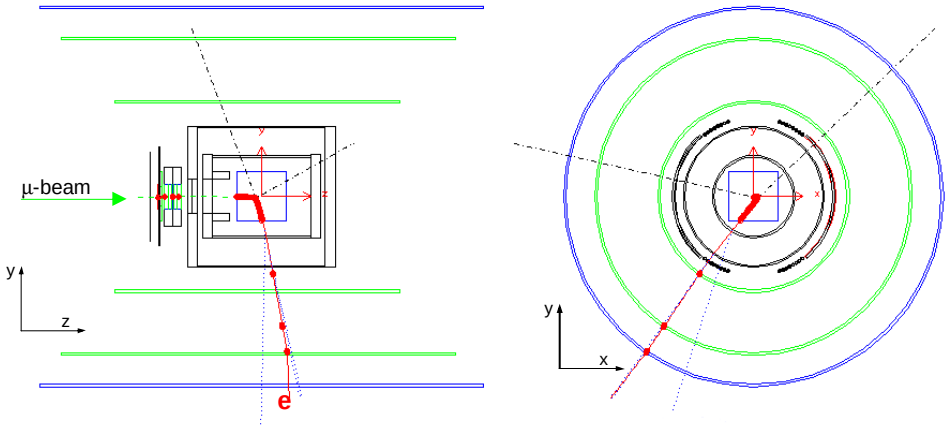

Figure 22: Simulated event showing the different detector components included in the present GEANT Monte Carlo. The red/green line shows the muon passing the muon entrance counters and stopping in the TPC. An electron (solid red line) and two neutrinos (dashed black lines) are created at the decay vertex. The electron is observed in the ePCs and the eSC, where the timing of the decay is recorded.

The Monte Carlo is based on our development for MuCAP, where it has been extensively used. The program is currently used as a design tool to guide the construction of various experimental sub-units. One study shows the large effect of the target density on the energy deposit of the beam muons on the stopping anode as shown in Fig. 23(a) for a 10 mm pad structure of the TPC. A muon typically deposits a large energy corresponding to the Bragg peak on the stopping anode. This critical study will ultimately define the optimal pad size for a given deuterium density, which was optimized for reasons given by muonic atoms and molecular kinetics. A similar comparison can be done for different pad sizes as shown in Fig. 23(b).

Beyond design studies, we intend to use the Monte Carlo to study specific systematic effects. The overall setup and idea of the simulation is a three-stage program sequence which starts with GEANT "data". The next stage applies specific detector properties, and then stores the final Monte Carlo events in the data format as will be delivered from electronic units. The resulting file can then be analyzed with standard analysis routines, which are identically used for "real" data.

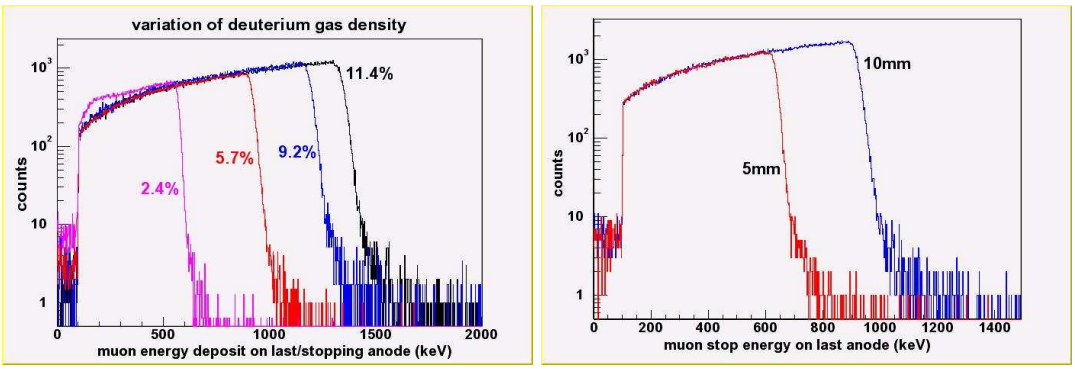

(a) (b)

Figure 23: (a) The energy deposition of beam muons on the stopping anode depending on the deuterium target density given in percent of liquid hydrogen density as calculated for a TPC with 10×10 mm^2 padsize.
(b) The energy deposit of beam muons on the stopping anode with two differently sized TPC pad sizes, 5×5 mm^2 and 10×10 mm^2 at a target density of 5.7% of liquid hydrogen density.

7 Statistics and Systematics

7.1 Statistics and Rates

The MuSun experiment will measure Λ_d to $< 1.5\%$. However, as it will become clearer from the error estimate in the later subsection 7.2, a precision of 1.2% seems to be achievable and will be used as the basis here. Thus $\delta\lambda = \lambda_\mu^- - \lambda_\mu^+$ has to be measured to a precision of 4.8 s^{-1}. If we assume the final expected 1 ppm error in the μ^+ decay rate from MuLan, $\delta\lambda_\mu^+ = 0.455$ s^{-1}, MuSun then has to measure the μ^- decay rate to $\delta\lambda_\mu^- = 4.8$ s^{-1}. This can be achieved with a statistics of $1.8{\times}10^{10}$ fully reconstructed μ^-. A similar, but somewhat smaller statistics of μ^+ events will be collected, which is a powerful systematics check, as most instrumental related systematics are identical for μ^- and μ^+ measured with the same apparatus and hence cancel.

Run		weeks beam time
300 K, phase 1		10*
30 K, phase 2		
commissioning and setup		8**
primary data taking	N_-: 1.8×10^{10}	10
	N_+: 1.2×10^{10}	6
systematics and calibration		6
total		40

Table 7: Statistics and beam time estimates. N_- (N_+) are the statistics of fully reconstructed μ^- (μ^+) decay events $\mu \to e\nu\bar{\nu}$ after all selection cuts have been applied. *We will split these weeks into two blocks of 5 weeks, one at the end of 2008 and the second at the beginning of 2009. **These weeks include the commissioning of the full setup and individual setup time in case of a non permanent location of the MuSun detector in the πE3 area. See also the comment on this in the text.

In phase 1 of the run plan the new pad TPC will be commissioned and several key systematic and physics issues will be investigated using a room temperature setup. Phase 2 is the full experimental setup operating at cryogenic temperatures. The setup time for this complex experiment, including pumping and cooling times and slow HV ramping is significant, if the apparatus has to be craned in and out before each experiment. If we can establish a dedicated area for the experiment as is requested in section 9.2, we will save at least 4 weeks of beam time and reduce considerably the risks related to repeated setup and dismantling stages each year. The measurement schedule will be detailed in the

beam time request later in this document. Once the full setup is commissioned, the experiment will require two 12 weeks data taking runs.

Selection criteria	Relative event fraction per selection step	Rate (kHz)
μSC entrance scintillator		27
& full pile-up protected $\mu SC \times \mu PC$	ϵ_1=0.81	22
& stop in TPC fiducial volume	ϵ_2=0.45	9.7
& fully reconstructed electron	ϵ_3=0.61	5.9

Table 8: Relative event fractions between each selection step and resulting event rates for the different cuts applied.

The translation of statistics into measuring time is based on the realized rates achieved in MuCap. Typically 2×10^9 events were collected in one week. Table 8 compiles the factors contributing to the final rates. We are optimizing the new setup to improve ϵ_2, because of the higher gas density. Moreover, the experiment will benefit from the increase in proton current at PSI anticipated during the next years.

The MuSun experiment will also derive essential information from the time distributions of capture and fusion products. Their statistics are estimated based on a total number of stopped muons N in the TPC calculated as

$$N = \frac{N_-}{\epsilon_3} \tag{19}$$

which, for $N_- = 1.8 \times 10^{10}$, amounts to $N = 3 \times 10^{10}$. A rough estimate of the expected time distributions and statistics are given in Fig. 24 and table 9.

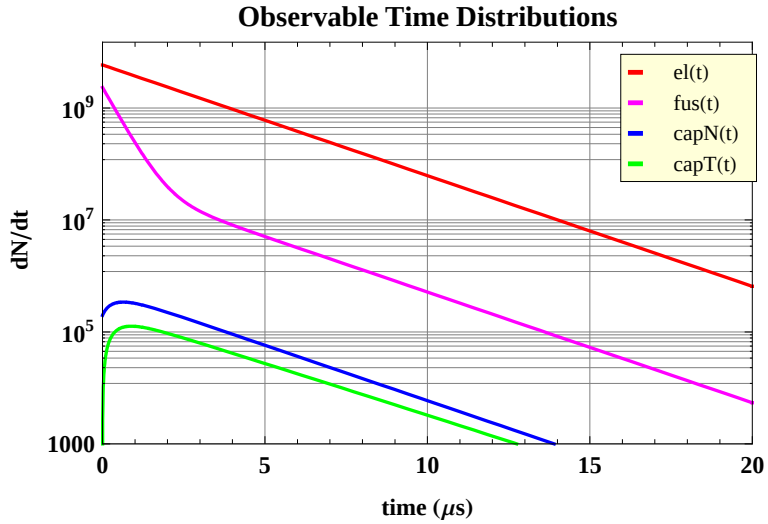

Figure 24: Observable time distributions for total good muon statistics of N= 3×10^{10}.

At $T = 30$ K and $\phi = 0.05$ the time spectrum (Fig. 24) of fusions shows two components: (i) a relatively strong, short time constant component with a lifetime that is governed by the μd hyperfine transition rate, and (ii) a relative weak, long time constant component with a lifetime that is governed by the muon dissappearance rate. Encoded in this time dependence of the fusion products are the $d\mu d$ molecular formation rates from the two hyperfine states (λ_q and λ_d) and the hyperfine transition rate between the two hyperfine states (λ_{qd}). Consequently, the detection of fusion products should enable the determination of the kinetics parameters λ_{qd}, λ_d and λ_d that are important in the extraction of the μd doublet capture rate Λ_d from the decay electron time spectrum.

An interesting feature of muonic deuterium is the combination of a very large hyperfine dependence of the muon capture rate with the similar magnitudes of the hyperfine transition rate and the muon

Process	Distribution	Yield/μ	Efficiency estimate	Total observed events
$\mu \rightarrow e\nu\bar{\nu}$	$el(t)$	0.9992	0.61	$1.8\times\ 10^{10}$
$dd\mu \rightarrow {}^3\mathrm{He}{+}n+\mu$	$fus(t)$	0.0305	1.00	$9.1\times\ 10^{8}$
$\mu + d \rightarrow n + n + \nu$	$cap_n(t)$	0.0015	0.01	$4.5\times\ 10^{5}$
$\mu{+}{}^3\mathrm{He}\rightarrow t + \nu$	$cap_T(t)$	$1.2\times\ 10^{-5}$	1.00	$3.6\times\ 10^{5}$
$\mu + N \rightarrow C^* + \nu$				$3.0\times\ 10^{5}$

Table 9: Total number of events for different processes based on N= 3.5×10^{10} and estimated detection efficiencies (column 3). The impurity capture events are based on typical MuCap conditions of 10^{-5} observed captures/muon. The impurity level should be reduced at T=30 K compared to the MuCap roomtemperature conditions.

disappearance rate. Consequently, the yield of capture neutrons (Fig. 24) first rises with time due to the hyperfine transition rate and then falls with time due to the muon disappearance rate. In principle, the detection of capture neutrons thus offers a method of determining both the hyperfine transition rate λ_{qd} and the capture rate from the quartet state Λ_q that are important in the extraction of the μd doublet capture rate from the decay electron time spectrum.

Initial simulations based on the detection of fusion products in the cryo-TPC reveal that sensitivities to λ_q, λ_d and λ_{qd} of several parts-per-thousand or better were achieved using the time information. For the capture neutrons the fitting procedure of simulated data results in a determination of λ_{qd} to $\pm3\%$ and to Λ_q to ±8 s^{-1}. The measurement of these parameters to such accuracies is well beyond the needed precision for the extraction of the μd doublet capture rate from the decay electron time spectrum. But given the long history of difficult and controversial interpretation of basic muon capture experiments due to muon-induced uncertainties, over-constraining the muon-induced kinetics will increase the confidence in the extraction of the weak capture rate Λ_d.

7.2 Systematics

Table 10 separates the systematic issues for the MuSun experiment into three categories. For each category the achieved precision of the first MuCap result is given in column 2, the anticipated precision of the final MuCap results (based on data already taken and ongoing analyses) is estimated in column 3 and the projected uncertainty of the MuSun experiment is presented in the last column. For systematics common to both experiments, only cases which differ between MuSun and MuCap are discussed below.

7.2.1 Clean Muon Stop

Fig. 25 displays four Monte Carlo generated muon stop signatures in the cryo-TPC. A pad TPC delivers a full three-dimensional sequence of the charge deposition in space, the figure shows the three two-dimensional projections. We are working on the algorithm to derive the basic muon parameters, i.e. the vector leading to the stopping point. The resolution in beam direction z is expected to be a fraction of a pad, based on the dE/dx information available. In y, a resolution of 1 mm, which corresponds to 250 ns, can be achieved. The x resolution needs to be optimized by simulating the pixel arrangement. We note that a tracking resolution of 5 mm is more than adequate for the experiment.

On the other hand we need to be careful regarding misreconstruction and tracking losses. The typical event signature of an incoming muon is very clean and simple, but some loss terms have to be controlled at the 100 ppm level. E.g. in the MuCap experiment, rare $\mu + p$ Coulomb scattering was carefully studied, as it potentially leads to a fake muon stop signature, where the large energy deposition expected at the end of the muon Bragg curve is faked by the recoil proton signal and the scattered muon escapes undetected. The full analog dE/dx information available in MuSun should highly suppress these events. Nevertheless, we will study them by Monte Carlo simulations and experimental data. Similar considerations are relevant for the overlap between the inital muon track and a fusion signal, discussed below.

Topic	MuCap 2007	MuCap Final	MuSun
Statistics	12.59	3.7	3.4
Similar for MuCap and MuSun			
chemical impurities	5.0	2	2*
analysis methods	5	2	2
$\mu + p$ scattering	3	1	1*
μ pilup veto inefficiency	3	1	1
MuCap only			
μd diffusion	1.6	0.5	
μp diffusion	0.5	0.5	
muon-induced kinetics	5.8	2	
MuSun only			
μd diff			0.5
^{1}H contamination			0*
fusion processes			1*
muon-induced kinetics			0.5*
total sys error	11.41	3.8	3.3
total error	13.32	5.3	4.7

Table 10: Comparison of the systematic uncertainties (in s^{-1}). Specific MuSun issues, different from the MuCap experimental conditions, are marked by * and evaluated in this section.

7.2.2 Chemical Gas purity

The purity requirements are estimated based on the experiments [1, 56]. The literature values for the transfer rates are given in table 11.

Nucleus	E (eV)	λ_{pZ} ($10^{10}s^{-1}$)	λ_{dZ} ($10^{10}s^{-1}$)
N	0.04	3.4 ± 0.7	14.5 ± 0.2
O	0.04	8.5 ± 0.2	6.3 ± 0.5

Table 11: Experimental muon transfer rates from μp and μd atoms to N and O, respectively. Transfer rates given for thermal energies, as thermalization is much faster than transfer at MuSun experimental conditions. The experimental references collected in the theoretical work [61].

Let us first estimate the requirements based on the MuCap experience. The published MuCap data had an observed yield of $Y_Z = 10.67$ ppm from the production data observed with a sensitivity of about 0.1 ppm. Calibration runs were taken with nitrogen-doped protium to determine how the observed disappearance rate deviates with the observed capture yield. This parameter, $\beta = \frac{\Delta\lambda}{Y_{EVH}}$, was found to be 1.30 ± 0.08 (s^{-1}/ppm). The efficieny for detecting a capture event was $\epsilon_N = 0.64$. The overall effect on the observed lifetime is $\alpha = \frac{\Delta\lambda}{c_N} = 96$ Hz/ppm. Accordingly the yield Y_{EVH} has to be measured or constrained to better than 1.5 ppm to limit $\Delta\lambda \leq 2$ Hz. This level of precision was achieved in all production runs. The main final error came from the uncertainty in the H_2O contribution and the relative contribution of humidity and nitrogen, which does not apply to MuSun as no H_2O is expected at cryogenic temperatures. It should be mentioned that the detection limit for detecting nitrogen by means of the chromatographic method was around 5 ppb.

In terms of the nitrogen concentration c_N the requirements are much harder in MuSun than in MuCap. According to α given above a precision $\Delta c_N \leq 20$ ppb is required for MuCap. In order to have the same correction $\Delta\lambda \propto Y_N$ for MuCap and MuSun, the following condition must be fulfilled.

$$\phi^{MuSun} \Delta c_N^{MuSun} \lambda_{dN} = \phi^{MuCap} \Delta c_N^{MuCap} \lambda_{pN}, \tag{20}$$

i.e. $\Delta c_N^{MuSun} = \Delta c_N^{MuCap}/21 \approx 1$ ppb.

In summary, it is very likely that we will achieve the required 1 ppb purity at cryo temperatures. However, the explicit verification of this fact will be hard. It requires to determine ΔY_N to 1 ppm or

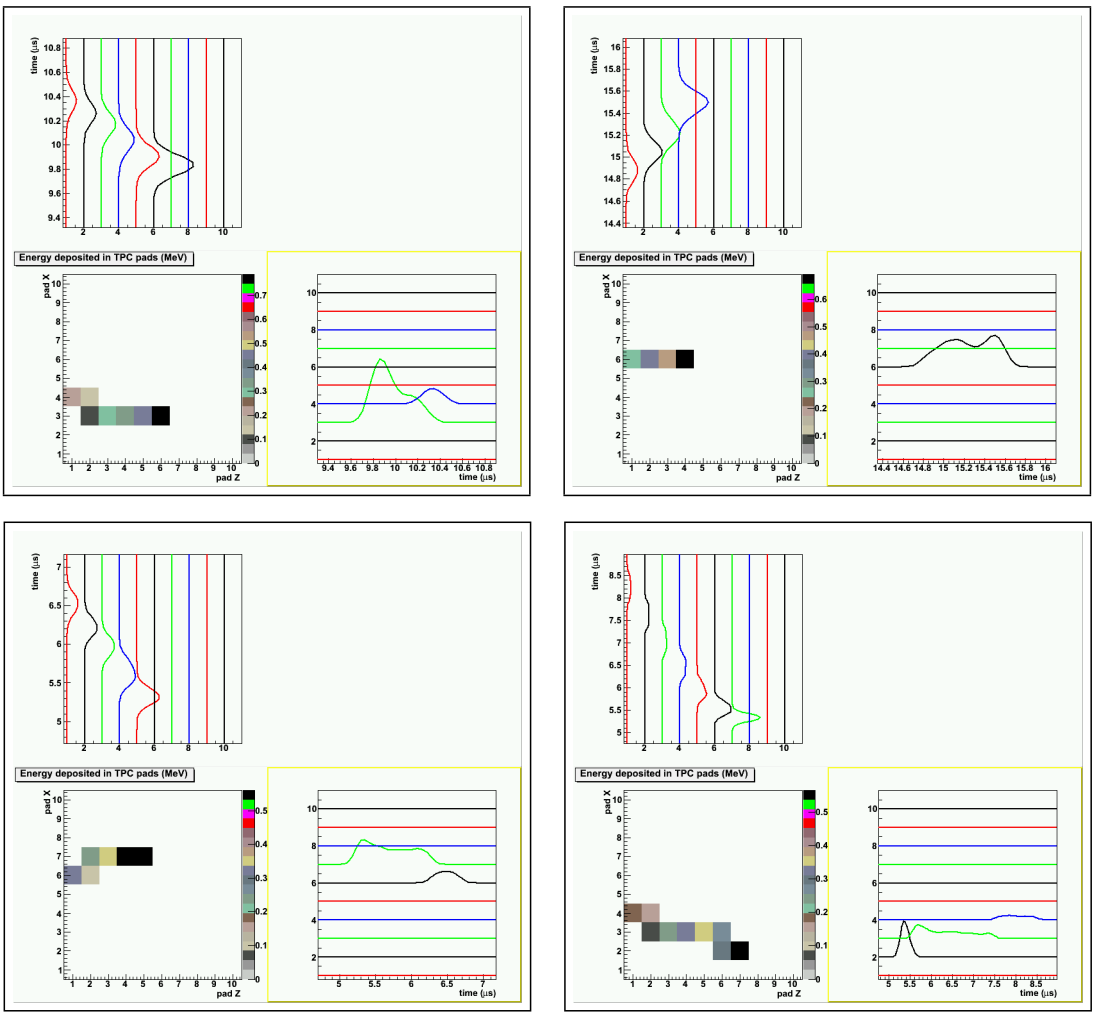

Figure 25: Four Monte Carlo generated muon stop signatures. The original fully three-dimensional information on charge deposition in the TPC is displayed in the 2-dimensional projections.

alternatively Δc_N to 1 ppb. The former condition was easily met in MuCap, the latter condition was not reached and an upgraded getter for the chromatography system is envisioned.

7.2.3 Gas Chromatography

To control the cleaning conditions both chromatography and online detection method are planned. Online humidity detector will control the moisture level without design modifications. To increase the sensitivity and precision of gas chromatographic method an additional subsystem for accumulation of impurities under cryogenic conditions is proposed. A N_2 getter will be placed directly in the CHUPS flow. In this way several 1000 l of D_2 would be passed through this getter per day, dramatically increasing the sensitivity compared to our 20 l typical gas samples. The collected impurity enriched gas will then be analyzed by the gas chromatograph and a sensitivity at sub-ppb level is expected.

7.2.4 Monitoring by Particle Detection

MuCap [59] developed a powerful method to detect capture recoils inside the TPC following muon transfer and capture on trace impurities in the protium gas. This allowed for continuous in-situ monitoring of the target purity over periods of several months. Applying the same method for MuSun is a technical challenge. MuCap had the ideal situation that the main reactions had pure neutral final states only and the maximum muon energy deposition on the TPC anode was below 250 keV, leaving

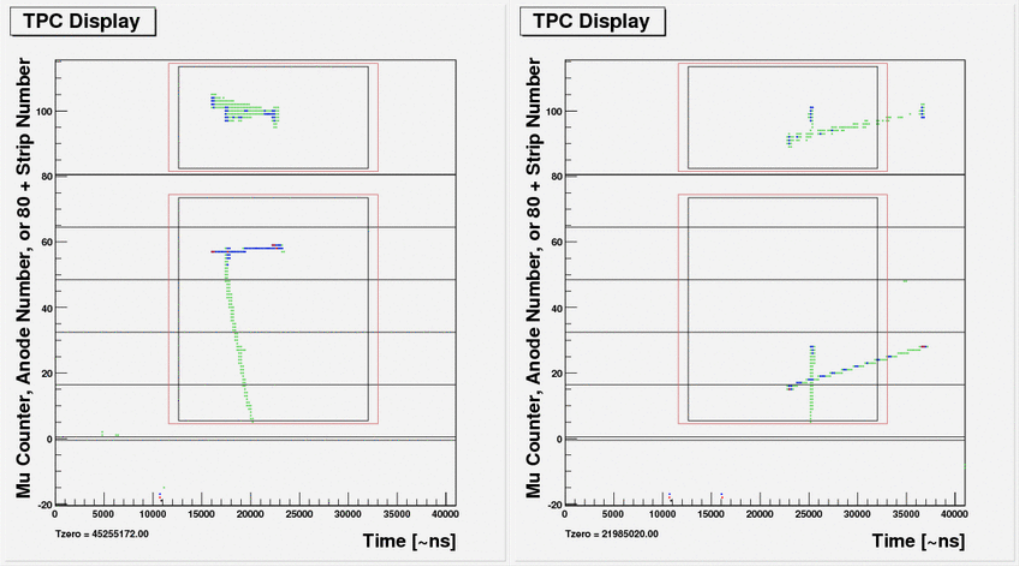

Figure 26: Two candidate events for a muon stopping in hydrogen with a subsequent muon capture on a nitrogen nucleus, leading to a charged particle track emmitted from the point of capture. The information is taken from the MuCap data and shows the $z-y$ (lower box) and $x-y$ projections of tracks in the TPC obtained from the drift time, anode and cathode information.

the 300-500 keV capture recoils cleanly separated from background. As shown in Fig. 11 a variety of charged fusion recoils are produced in pure D_2 and the muons can deposit energies up to 1 MeV (Fig. 23). Thus excellent resolution and full analog readout are essential in trying to identifying rare nitrogen capture events. Under the MuSun conditions, the ^{3}He background (Fig. 11) can be reduced 14 fold by the combination of a delayed time window after muon stop (where the fusion intensity has dropped) and by rejecting capture candiates if a decay electron is observed. It remains to be experimentally tested whether 1 ppb sensitivity to nitrogen can be achieved with such analysis cuts.

But more likely an additional tag (X-ray, capture topology in cryo-TPC, capture neutron) is required. If the tagging efficiency $\kappa \approx 0.01$, then we would expect some 1000 tagged capture events over the whole run. Probably a ^{3}He suppression by the tag by an order of magnitude is sufficient. We are studying configuration a), where the additional tagging detector is part of the main setup, which has the price of reducing its solid angle, or configuration b), where it is positioned close to the TPC vessel wall and a dedicated run without the electron tracker is performed. We will modify the beam pipe such that the electron tracker can be rolled upstream, and the new detectors placed around the TPC, which is rolled a bit downstream relative to its nominal detection position. Additional detectors can be placed at R_o=390 mm and R_i=185 mm for configuration a) and b), respectively. Naively the ratio of solid angles is $(\frac{R_o}{R_i})^2 \approx 4$ and the signal/noise is favorable for configuration b). The tagging processes considered are the following:

- Capture recoil topology in the TPC. We have been analyzing charged particle emission after muon capture in nitrogen doped data from MuCap. According to our knowledge, there is not reliable literature data on this process. We find that about 14% of capture events with a initial nuclear recoil above 300 keV exhibit long range charged particle tracks (Fig. 26), probably dominantly from protons. Currently these selected events are being parametrized. They will be used as input for Monte Carlo simulations in order to understand the possibility of efficiently detecting and identifying such events with different cryo-TPC pad geometries.

- X-ray and neutron emission during transfer and capture. During μp to μZ transfer muonic Lyman X-rays in the range 102-131 keV are emitted with nearly 100% probablity. These could be detected with gamma detectors, e.g. a 10 mm thick NaI slab placed in the isolation vacuum would be an efficient detector. Additionally nuclear X-rays and neutrons are emitted during the capture process, which also could serve as tags to discriminate against fusion events.

While the solid angle for different detector options can be easily calculated, the signal to background ratio is best explored experimentally. We plan to prepare several test detectors for our stage 1 measurement to optimize the tagging method.

We also plan protium measurements during the final stage 2 measurements, where the required capture yield sensitivity is easily obtained. That will allow for an improved understanding of the surface dependent cryo-pumping of our cold target and will calibrate the various purity monitoring methods.

7.2.5 Isotopic Gas Purity

The up-to-now most precise μd experiment [3] measured the effect of ^{1}H impurities in their liquid deuterium target and reported a shift in their measured decay rate of 12 s^{-1} for a hydrogen contamination of $c_p \approx 1.6\times10^{-3}$. As the MuSun target density ϕ is more than 10 times smaller, the effect is expected to be reduced by an order of magnitude at the same c_p. Moreover, with the Deuterium Separation Unit we will be able to produce deuterium with $c_p < 10^{-6}$, essentially eliminating this correction. The use of hydrogen free deuterium will also suppress the $pd\mu$ low energy peak in Fig. 11 and thus improve our detection capablities for nitrogen capture.

7.2.6 Uncertainties Introduced by the Muon-induced Kinetics

The systematic impact of these kinetic effects has been carefully considered in the design of the experiment. As discussed in section 5.3 in the optimized experiment at T = 30 K and ϕ=0.05 the uncertainties from the kinetics are reduced to less than $\delta\Lambda_d = 1$ s^{-1}, which is significantly below the total precision for this proposal and therefore of no concern.

7.2.7 Fusion Processes

As discussed above the muon-catalyzed-fusion processes serve as important monitors of the underlying muon-induced kinetics. However, at the nominal ϕ=0.05, the probability for emission of charged fusion products is several percent. Does the interference of these tracks with the muon track distort the $\mu - e$ time distribution?

Let us assume that this interference leads to muon losses with the probablity $\eta(t_f)$, depending on the time after muon stop t_f, when the fusion occurs. The probablity to lose an electron decay at time t_e is then

$$P_{loss}(t_e) = \int_0^{t_e} \eta(t_f)(\phi\lambda_q N_q(t_f) + \phi\lambda_d N_d(t_f))e^{\lambda_\mu^+ t} dt_f. \quad (21)$$

The time distribution under the integral is the solution of the kinetic equations Eq. 11, setting λ_μ^+= 0 (as the muon decays only at t_e). Conservative estimates of the impact of this time dependent effect indicate that the loss probablity $\eta(t_f)$ should be kept below about 1%. Muon stop reconstruction at this level can be achieved with appropriately defined muon stop cuts. We plan to study this question with Monte Carlo and during our test run. It is worth noting that the fusion neutron distribution would directly reflect potential muon losses due to the ^{3}He+n branch of the fusion distribution. If muons are lost because of the above mentioned effect, the observed distribution $fus(t)$ would be multiplied by a factor $(1 - \eta(t_f))$, providing a direct experimental handle on $\eta(t_f)$.

7.2.8 Polarization of μd atoms

As described in detail in Appendix 11.1, a potential complication in the time spectrum of the decay electrons from the μ^-d atoms is the presence of a μSR signal. Using a Monte Carlo simulation of the μSR modulation – with estimates of the muon beam polarization, atomic cascade depolarization, D_2 collisional depolarization, and the anisotropy of the detection efficiency – we studied the effects of the μSR signal on the electron time spectrum. Based on our experience with μSR effects in the MuLan experiments, we expect the effects on Λ_d to be considerably smaller than the proposed precision ±6 s^{-1}.

8 Measuring Program

8.1 Stage 1 - Room Temperature TPC

The experiment will proceed in two stages. First we will prepare a prototype of the new pad TPC. The pad plane layout and Frisch grid will be identical to the final TPC, but the chamber will operate at room temperature at density ϕ=1% (MuCap conditions). This central detector will be a reconfiguration of the second TPC, which the collaboration prepared for the MuCap experiment [5]. For this first stage, we request 10 weeks of beam time for commissioning and physics running with this new chamber. Essential technical goals of this stage include:

- Demonstrate excellent resolution and muon identification with new TPC operated as ionization chamber.
- Identification and separation of fusion recoils.
- Full analog readout of whole TPC in untriggered mode.

The physics goals are as follows

- Measurement of the tranfer rate from deuterium to nitrogen.
- Attempt to monitor impurities by detection of capture events in the presence of fusion background with dedicated set-up.
- Observation of residual polarization of muons in the μd quartet state.
- In addition, depending on the advanced status of the setup, also an attempt for a first capture rate measurement can be envisioned although the items above are of more relevance in this period.

The general goal of this phase is to collect data required to optimize the final detector in terms of performance and of systematic issues generated by physics background. Moreover, new components should be tested and optimized before building the final detector which is integrated in a complex cryo system. During the fall run, if the new pad TPC is ready, we would primarely work on commissioning this new detector and on dedicated experiments with auxilary detectors to develop the best method to tag impurities. The electron tracker then could be added during the shut-down period, to prepare for the systematically essential transfer rate experiment after the shutdown. The full analog readout of the TPC in real time will be implemented already in 2008.

The collaboration is working on an optimized schedule for 2008 and will discuss a more detailed plan at the PAC meeting.

8.2 Stage 2 - Cryo-TPC and Λ_d Determination

By fall of 2009 the high density cryo-TPC should be ready and a first commissioning run is planned. The further requests will depend on the experience gained and whether a permanent experimental cage can be established for the MuSun experiment in the πE3 area, which would very significantly increase the scheduling flexibility. If the new detector works as expected and the systematic issues outlined in section 7.2 are under control, we would focus on the determination of the capture rate Λ_d to a precision of 1.2%. The required statics can be achieved in two- to three 10-12 weeks runs including set-up, distributed over a two-years period. As has been successful in MuCap we usually split each run into main μ^- data taking, μ^+ reference data and systematic studies, as significant systematic cancellation occur when comparing data taking within a run period.

[5] The first MuCap TPC, used in our ultrapure protium measurements, will be left untouched in order to keep the possibility of running with the protium conditions again, if ever necessary.

9 Organization

9.1 Responsibilities and Budget

The division of responsibilities between the participating institutions will follow the lines depicted in table 12, though there will be, as in the past for MuCap, significant collaborative overlap. We do not elaborate on the expertise and resources of the individual institutions, as the present plan broadly follows the concept which has successfully worked for MuCap over many years.

System	responsible institutions						
	PNPI	**UIUC**	**PSI**	**UKY**	**BU**	**UCL**	**RU**
Detectors		⊙		⊙		⊙	
TPC	⊙	⊙					
Cryogenic system	⊙		⊙				
Gas and purification system	⊙		⊙				
Front end electronics	⊙	⊙	⊙		⊙	⊙	
DAQ + computers				⊙			⊙

Table 12: Main hardware responsibilities of participating institutions.

For computing requirements, we plan to maintain and upgrade the existing on-line analysis cluster developed by the MuCap and MuLan Collaborations to cope with the very significant data volume. We request about 100 TB of data storage space on the PSI archive over the next three years. We expect that the bulk of the off-line analysis will be performed at the US National Center for Supercomputing Application (NCSA), where we have developed analysis software structures and experience over the last years and have obtained significant allocations of several 100k CPU hours on the required multi-node system.

The equipment costs can be kept low, because MuSun benefits from much higher investments by MuCap and MuLan, providing important experimental infrastructure. This includes the MuCap detectors, electronics, high vacuum and purification system and the MuLan kicker, FADC electronics, as well as the DAQ infrastructure of both experiments, to name a few major examples. We estimate the overall new equipment expenses for this experiment to be of the order of 350k CHF. The main cost driver will be the cryo-TPC, which also has a significant labor-intensive component. Based on past MuCap/MuLan experience, additional operating expenses for running the experiment (travel, shipping, storage media, incidentals like chamber gas, etc.) amount to about 100k CHF per year. The collaborating institutions have discussed the new project with their respective funding agencies (mainly the National Science Foundation in the US and the Russian Academy of Sciences in Russia) and received encouraging responses. Naturally, acceptance of this proposal by the PAC is critical to go forward with full funding proposals.

We welcome additional groups to join the MuSun experiment.

9.2 Request to PSI

Our requests to PSI are based on the PSI expertise, which was critical to the success of the MuCap experiment. Different from MuCap, the PNPI group will assume the main responsibility for the new cryo-TPC development, with direct support from UIUC and infrastructure from PSI as is available.

The financial request to PSI is based on the MuCap experience and amounts to 20 kCHF/year for equipment costs and 30 kCHF/year for running costs. The equiment budget includes contributions to the new cryogenic system, the gas handling and purification system, and the 100 kV supply (15k CHF), which is required for the main drift field. The running costs involve magazine items, small orders and partial support of the PNPI visits (guest house, travel support).

As described earlier, MuSun will require several weeks of set-up time before the data taking. A permanent location of the experiment in the annex of πE3 beamline area would greatly reduce technical risks and enhance efficiency, allowing for a flexible work schedule for the teaching faculty members within our collaboration.

9.3 Project Schedule

Fig. 27 provides a preliminary overview of the project schedule. The present version is a work-in-progress and will be updated as the planning evolves. The project has two main directions. In 2008, we plan to build the room temperature prototype TPC (proto-TPC) and perform first measurements at the end of the running year. These measurements are essential for the optimization of the final chamber design and for the overall experiment. We are optimistic that we can achieve these goals within one run. In that case we would not need the additional 5 weeks early 2009, which are mentioned in the beam request. In parallel, we will perform basic R&D towards the cryo-TPC, including the detector itself, the cryogenic vessel, window and feedthrough and the overall concept. Based on the learning experience of the fall 2008 run, we plan to proceed with the construction of the final apparatus early in 2009 and have a first commissioning run in fall 2009.

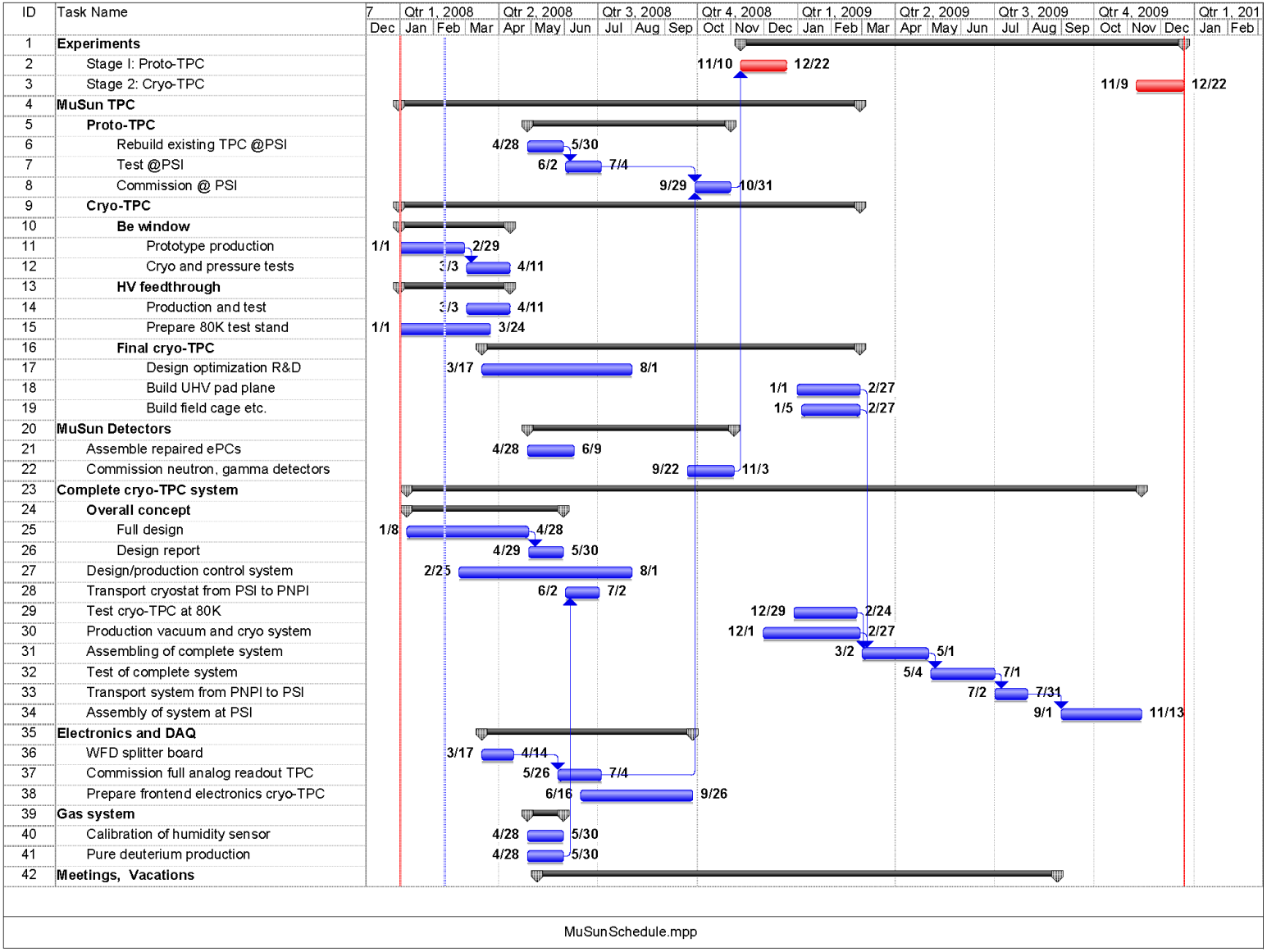

Figure 27: Preliminary project schedule gantt chart

10 References

[1] V. A. Andreev et al. Measurement of the Rate of Muon Capture in Hydrogen Gas and Determination of the Proton's Pseudoscalar Coupling g_P. *Phys. Rev. Lett.*, 99:032002, 2007.

[2] V. Bernard, Norbert Kaiser, and Ulf-G. Meissner. Chiral dynamics in nucleons and nuclei. *Int. J. Mod. Phys.*, E4:193–346, 1995.

[3] G. Bardin et al. A measurement of the rate of muon capture in liquid deuterium by the lifetime technique. *Nucl. Phys.*, 1986.

[4] M. Cargnelli et al. Measurement of the muon capture rate in gaseous deuterium. In *Proceedings of the XXIII Yamada Conf. on Nuclear Weak Processes and Nuclear Structure, Osaka, Japan*, 1989.

[5] S. Ando, T. S. Park, K. Kubodera, and F. Myhrer. The μ^-d capture rate in effective field theory. *Phys. Lett.*, B533:25–36, 2002.

[6] Jiunn-Wei Chen, Takashi Inoue, Xiang-dong Ji, and Ying-chuan Li. Fixing Two-Nucleon Weak-Axial Coupling $L_{1,A}$ From μ^-d Capture. *Phys. Rev.*, C72:061001, 2005.

[7] B. Aharmim et al. Measurement of the ν_e and total ^{8}B solar neutrino fluxes with the Sudbury Neutrino Observatory phase I data set. *Phys. Rev.*, C75:045502, 2007.

[8] Tae-Sun Park, Kuniharu Kubodera, Dong-Pil Min, and Mannque Rho. The solar proton burning process revisited in chiral perturbation theory. *Astrophys. J.*, 507:443–453, 1998.

[9] S. Nakamura, T. Sato, V. Gudkov, and K. Kubodera. Neutrino reactions on the deuteron. *Phys. Rev.*, C63:034617, 2001.

[10] S. Ando, Y. H. Song, T. S. Park, H. W. Fearing, and K. Kubodera. Solar-neutrino reactions on deuteron in effective field theory. *Phys. Lett.*, B555:49–56, 2003.

[11] Malcolm Butler, Jiunn-Wei Chen, and Petr Vogel. Constraints on two-body axial currents from reactor antineutrino deuteron breakup reactions. *Phys. Lett.*, B549:26–31, 2002.

[12] A. Gardestig and D. R. Phillips. How low-energy weak reactions can constrain three-nucleon forces and the neutron neutron scattering length. *Phys. Rev. Lett.*, 96:232301, 2006.

[13] T. S. Park et al. Parameter-free effective field theory calculation for the solar proton fusion and hep processes. *Phys. Rev.*, C67:055206, 2003.

[14] Kuniharu Kubodera and Tae-Sun Park. The solar He p process. *Ann. Rev. Nucl. Part. Sci.*, 54:19–37, 2004.

[15] Steven Weinberg. Nuclear forces from chiral lagrangians. *Phys. Lett.*, B251:288–292, 1990.

[16] Steven Weinberg. Effective chiral lagrangians for nucleon - pion interactions and nuclear forces. *Nucl. Phys.*, B363:3–18, 1991.

[17] Steven Weinberg. Three body interactions among nucleons and pions. *Phys. Lett.*, B295:114–121, 1992.

[18] Shung-ichi Ando, Fred Myhrer, and Kuniharu Kubodera. Capture rate and neutron helicity asymmetry for ordinary muon capture on hydrogen. *Phys. Rev.*, C63:015203, 2001.

[19] S. Nakamura et al. Neutrino deuteron reactions at solar neutrino energies. *Nucl. Phys.*, A721:549–552, 2003.

[20] D. R. Phillips and T. D. Cohen. Deuteron electromagnetic properties and the viability of effective field theory methods in the two-nucleon system. *Nucl. Phys.*, A668:45–82, 2000.

[21] A. Gardestig and D. R. Phillips. Using chiral perturbation theory to extract the neutron neutron scattering length from $\pi^-\mathrm{d} \to \mathrm{nn}\gamma$. *Phys. Rev.*, C73:014002, 2006.

[22] Norbert Kaiser, R. Brockmann, and W. Weise. Peripheral nucleon nucleon phase shifts and chiral symmetry. *Nucl. Phys.*, A625:758–788, 1997.

[23] E. Epelbaum, Walter Gloeckle, and Ulf-G. Meissner. Nuclear forces from chiral Lagrangians using the method of unitary transformation. II: The two-nucleon system. *Nucl. Phys.*, A671:295–331, 2000.

[24] M. C. M. Rentmeester, R. G. E. Timmermans, J. L. Friar, and J. J. de Swart. Chiral two-pion exchange and proton proton partial-wave analysis. *Phys. Rev. Lett.*, 82:4992–4995, 1999.

[25] D. R. Entem and R. Machleidt. Accurate charge-dependent nucleon-nucleon potential at fourth order of chiral perturbation theory. *Phys. Rev.*, C68:041001, 2003.

[26] N. Tatara, Y. Kohyama, and K. Kubodera. Weak interaction processes on deuterium: Muon capture and neutrino reactions. *Phys. Rev.*, C42:1694–1717, 1990.

[27] J. Adam, E. Truhlik, S. Ciechanowicz, and K. M. Schmitt. Muon capture in deuterium and the meson exchange current effect. *Nucl. Phys.*, A507:675–697, 1990.

[28] M. Doi, T. Sato, H. Ohtsubo, and M. Morita. Effect of meson exchange current on deuteron - muon capture. *Nucl. Phys.*, A511:507, 1990.

[29] W. J. Marciano and A. Sirlin. Radiative corrections to beta decay and the possibility of a fourth generation. *Phys. Rev. Lett.*, 56:22, 1986.

[30] Andrzej Czarnecki, William J. Marciano, and Alberto Sirlin. Electroweak radiative corrections to muon capture. *Phys. Rev. Lett.*, 99:032003, 2007.

[31] S. Ando et al. Neutron beta decay in effective field theory. *Phys. Lett.*, B595:250–259, 2004.

[32] I.-T. Wang et al. Muon Capture by Deuterons. *Phys. Rev.*, 139:0B1539, 1965.

[33] A. Bertin, A. Vitale, A. Placci, and E. Zavattini. Muon capture in gaseous deuterium. *Phys. Rev.*, D8:3774–3793, 1973.

[34] P. Kammel et al. First observation of muonic hyperfine effects in pure deuterium. *Phys. Rev.*, A28:2611–2622, 1983.

[35] B. Aharmim et al. Electron energy spectra, fluxes, and day-night asymmetries of ^{8}B solar neutrinos from the 391-day salt phase SNO data set. *Phys. Rev.*, C72:055502, 2005.

[36] S. Nakamura et al. Neutrino deuteron reactions at solar neutrino energies. *Nucl. Phys.*, A707:561–576, 2002.

[37] Malcolm Butler, Jiunn-Wei Chen, and Xinwei Kong. Neutrino deuteron scattering in effective field theory at next-to-next-to-leading order. *Phys. Rev.*, C63:035501, 2001.

[38] B. Mosconi, P. Ricci, E. Truhlik, and P. Vogel. Model dependence of the neutrino deuteron disintegration cross sections at low energies. *Phys. Rev.*, C75:044610–044615, 2007.

[39] John N. Bahcall and M. H. Pinsonneault. What do we (not) know theoretically about solar neutrino fluxes? *Phys. Rev. Lett.*, 92:121301, 2004.

[40] R. Schiavilla et al. Weak capture of protons by protons. *Phys. Rev.*, C58:1263, 1998.

[41] Jiunn-Wei Chen, Karsten M. Heeger, and R. G. Hamish Robertson. Constraining the leading weak axial two-body current by SNO and Super-K. *Phys. Rev.*, C67:025801, 2003.

[42] K. I. T. Brown, M. N. Butler, and D. B. Guenther. Constraints on proton-proton fusion from helioseismology. 2002. nucl-th/0207008.

[43] A. B. Balantekin and H. Yuksel. Neutrino physics and nuclear axial two-body interactions. *Int. J. Mod. Phys.*, E14:39–46, 2005.

[44] A. B. Balantekin and H. Yuksel. Constraints on axial two-body currents from solar neutrino data. *Phys. Rev.*, C68:055801, 2003.

[45] A. W. P. Poon. Review of solar and reactor neutrinos. *Int. J. Mod. Phys.*, A21:1855–1868, 2006.

[46] R. Machleidt and I. Slaus. The nucleon nucleon interaction. *J. Phys.*, G27:R69, 2001.

[47] D. E. Gonzalez Trotter et al. Neutron-deuteron breakup experiment at E(n) = 13-MeV: Determination of the $^1S_0$ neutron-neutron scattering length a_{nn}. *Phys. Rev.*, C73:034001, 2006.

[48] V. Huhn et al. New investigation of the neutron neutron and neutron proton final state interaction in the n d breakup reaction. *Phys. Rev.*, C63:014003, 2001.

[49] Robert B. Wiringa, V. G. J. Stoks, and R. Schiavilla. An accurate nucleon-nucleon potential with charge independence breaking. *Phys. Rev.*, C51:38–51, 1995.

[50] Steven C. Pieper and Robert B. Wiringa. Quantum monte carlo calculations of light nuclei. *Ann. Rev. Nucl. Part. Sci.*, 51:53–90, 2001.

[51] A. Gardestig. Chiral $\mathcal{O}(Q^4)$ two-body operators for s-wave pion photoproduction on the NN system. *Phys. Rev.*, C74:017001, 2006.

[52] P. Ackerbauer et al. A precision measurement of nuclear muon capture on He-3. *Phys. Lett.*, B417:224–232, 1998.

[53] J. J. Simpson. Half-life of tritium and the Gamow-Teller transition rate. *Phys. Rev.*, C35:752–754, 1987.

[54] A. P. Serebrov et al. Neutron lifetime measurements using gravitationally trapped ultracold neutrons. 2007. nucl-ex/0702009.

[55] W. H. Breunlich, P. Kammel, J. S. Cohen, and M. Leon. Muon-catalyzed fusion. *Ann. Rev. Nucl. Part. Sci.*, 39:311–356, 1989.

[56] D.V. Balin et al. High Precision Study of Muon Catalyzed Fusion in D_2 and HD Gases. *PNPI Preprint*, 2729, 2007. http://www.npl.uiuc.edu/elog/mucap/MuCap+Notes/080129_181009/mcf_9_9_07_.pdf.

[57] P. Kammel et al. First observation of hyperfine transitions in muonic deuterium atoms via resonant $d\mu d$ formation at 34-K. *Phys. Lett.*, B112:319–322, 1982.

[58] J. Zmeskal, P. Kammel, A. Scrinzi, W. H. Breunlich, M. Cargnelli, J. Marton, N. Nägele, J. Werner, W. Bertl, and C. Petitjean. Muon-catalyzed *dd* fusion between 25 and 150 K: Experiment. *Phys. Rev.*, A42(3):1165–1177, 1990.

[59] V. A. Ganzha et al. A circulating hydrogen ultra-high purification system for the mucap experiment. *Nucl. Instrum. Meth.*, A578:485–497, 2007.

[60] M. Suter et al. Advances in particle identification in AMS at low energies. *Nuclear Instruments and Methods in Physics Research*, B259:165–172, 2007.

[61] Arnaud Dupays. Isotopic Effects in the Muon Transfer from pμ and dμ to Heavier Atoms. *Phys. Rev. Lett.*, 93(4):043401, Jul 2004.

[62] H. Uberall. Hyperfine effects in capture of polarized muons. *Phys. Rev.*, 114:1640–1645, 1959.

[63] V. P. Dzhelepov and V. V. Fil'chenkov. Experimental investigations of mu-atomic and mu-molecular processes in hydrogen on the jinr synchrocyclotron. *Atomic Energy*, 55:819–842, 1983.

[64] G. F. Binko et al. Measurement of residual polarization of negative muons in gaseous deuterium at 10-ATM pressure. *JETP Lett.*, 49:544, 1989.

[65] V. M. Bystritskii et al. Measurement of the residual polarization of negative muons in gaseous hydrogen. *JETP*, 53(3):426–432, 1981.

11 Appendix

11.1 Polarization and Muon Spin Rotation

A potential complication in the time spectrum of the decay electrons from the μ^-d atoms is the presence of a μSR signal. If the μ^-d atoms have a non-zero polarization, their spins will precess and relax in the environmental magnetic field of the muon stopping volume (the precession frequencies are $\omega_{3/2}/B = 0.026$ μs/G for the quartet state and $\omega_{1/2}/B = 0.034$ μs/G for the doublet state). Due to the directional correlation between the muon spin vector and the electron momentum vector this imparts a μSR modulation onto the time spectrum of the decay electrons. Note such effects were absent for the singlet μ^-p atoms in the muCap experiment.

For a perfectly isotropic detector this μSR signal would vanish in the summed time spectrum of electrons emitted in all directions. However, any anisotropies in the detection efficiency about the μ-spin axis will lead to a μSR modulation of the electron time spectrum. Below we describe our simulations of the influence of the μSR signal, both the spin precession and the spin relaxation, on the determination of the μ^-d effective lifetime from the electron time spectrum. Our simulations are based on estimates of: (1) the μ^- polarization of the cloud muon beam, (2) the initial μ^- depolarization in the atomic cascade process, (3) the subsequent μ^- depolarization via collisions with D_2 molecules, and (4) the anisotropy in the electron detection efficiency.

1. for the πE3 channel the available data for negative cloud muons with momenta 35-45 MeV/c imply a polarization of about 25% at 32.6 MeV/c. This result is consistent with our own determination of the beam polarization for positive cloud muons at 32.6 MeV/c, which yielded a value of 22%. Herein, we assume a value of 25% for the negative cloud muon beam polarization.
2. the particular case of muon depolarization in μ^-d cascade was considered by Uberall [62] and Dzhelepov and Fil'chenkov [63]. Using a spin-orbit depolarization factor of 1/6 from Ref. [63] and spin-spin depolarization factors of 10/27 ($F = 3/2$ state) and 1/27 ($F = 3/2$ state) from Ref. [62], we obtain overall depolarization factors of 0.17 and 0.03 for the $F = 3/2, 1/2$ hyperfine states, respectively. [6] Herein, we assume a quartet state depolarization factor of 0.17 and ignore the much smaller effects of the doublet state polarization.
3. after formation of ground state μ^-d atoms their initial polarization will further relax due to exchange collisions with the surrounding D_2 molecules. Note, both collisions which (a) change the μ^-d atom's spin and (b) change the μ^- spin projection will contribute to relaxation, and therefore the rate of spin relaxation can exceed the measured hyperfine transition rate. Herein, we assume value of 2.3×10^6 s^{-1} at $\phi = 0.05$ from Ref. [63] for the relaxation rate of the quartet state.
4. the detector anisotropy has contributions including detector solid angle variations and detector intrinsic efficiency variations and was estimated from our experience with the muCap setup. Herein, we shall assume an anisotropy of $\epsilon = 0.02$ in the detection efficiency.

In order to estimate the influence of a μSR signal on the determination of the μ^-d lifetime we performed a Monte Carlo simulation. Electron time spectra were generated according to a exponential decay law with a μSR modulation according by

$$N \exp(-t/\tau)(1 + A \exp(-t/\tau_R) \cos(\omega t + \phi)) \tag{22}$$

where τ is the muon's effective lifetime and A, ω, ϕ and τ_R are the amplitude, frequency, phase and relaxation constant of the μSR signal. The amplitude $A = 0.013$ was determined by the product of the initial beam polarization (0.25), atomic cascade depolarization (0.17) and the asymmetry coefficient of the muon spin/electron momentum directional correlation (0.3).

To incorporate the detector anisotropy ϵ we generated (i) a "forward hemisphere" time spectrum with phase $\phi = 0$ and total counts $N_o/2$ and (ii) a "backward hemisphere" time spectrum with phase $\phi = \pi$ and total counts $(N_o/2)\times(1 + \epsilon)$, and then summed the two time spectra. For $\epsilon = 0$ the μSR signal vanishes in the sum spectrum, whereas for $\epsilon > 0$ a diluted version of the individual μSR signals

[6] Unfortunately, the experimental data on μSR in deuterium is limited and confusing. Bin'ko *et al.* [64] studied μ^- depolarization in 300K, 10 Atm D_2 gas and reported an initial polarization of quartet atoms of (7.2±2.1)%. Bystritskii it et al. [65] studied μ^- depolarization in 300K, 40 atm D_2 gas and reported an initial polarization of quartet atoms of (1.0±0.9)%.

appears in the sum spectrum. Next the sum spectra were fit to extract the lifetime. In the first fitting procedure, the "worst case" scenario, we fit a single exponential, *i.e.* completely ignoring the time structure of the μSR signal. In the second fitting procedure, the "best case" scenario, we fit a single exponential with the μSR function, *i.e.* correctly incorporating the time structure of the μSR signal.

In the "worst case" scenario we found a lifetime shift of up to ± 10 ppm (equivalent to a shift in the doublet rate of about ± 5 s^{-1}). Note the shift in the fitted lifetime was correlated with the fit start time, the sinusoidal time dependence of the μSR signal inducing a sinusoidal time variation of the extracted lifetime with the fit start time. Also note that the omission of the μSR signal in the fits was obvious in the poor χ^2's and the large residuals for these fits.

In the "best case" scenario we found no shift in the fitted lifetime at the level of about ± 1 ppm. A small (sub ppm) increase in the statistical uncertainty on the fitted lifetime, that is presumably from the correlations with the μSR parameters, was, however, observed. In this fitting procedure the fit χ^2 was always acceptable.

In reality, we expect the true situation to fall between the "best case" and "best case" scenarios. While its impossible to exactly know the time structure of the μSR signal, the difference spectra between forward/backward hemispheres will obviously help in characterizing its time structure. In short, the μSR effect is not expected to be significant problem in the lifetime determination.

Glossary

Symbols

$\bar{\omega}$	Sticking probability, i.e. the fraction of the $dd\mu$ fusion events where the muon remains in a bound state with the ^{3}He.
β	Branching fraction of the $dd\mu$ fusion to the ^3He+n channel normalized to the possible ^3He+n and $p+t$ final states.
$\hat{d}^R$	Low energy constant, describing the $2N$ axial currents in ChPT. Analogous to L_{1A} in the pionless EFTs.
λ_μ^+	Lifetime of the positive muon μ^+.
Λ_T	Partial muon capture rate on a ^{3}He with a trition in the final state.
λ_{dZ}	The transfer rate of a μ^- from a bound $\mu^- d$ state to a bound μ^-Z state, where Z is the atomic number of an impurity atom. The transfer rate λ_{pZ} refers to the analogous process, where the μ^- is initially bound by a proton. These rates are proportional to the concentration of the impurity element in the target gas, C_Z.
ϕ	The density of the deuterium target gas relative to the density of liquid hydrogen.
a_{nn}	Neutron-neutron scattering length.
C_Z	The atomic concentration of a Z $>$ 2 impurity relative to deuterium concentration in the target gas. A critical example of such an impurity is nitrogen.
L_{1A}	Low energy constant from pionless EFT describing the μ^- capture on the deuteron and other weak reactions in the $2N$ system. The capture rate Λ_d is parameterized by $\Lambda_d = a + b\ L_{1A}$.
q	Initial quartet fraction $\frac{2}{3}$, i.e. the fraction of muons that end up in the quartet hyperfine state of the μd ground state after the muon stops in deuterium and cascades down to the 1S state.
λ_{dq}	Hyperfine transition rate from the doublet to the quartet μd state.
λ_d	$dd\mu$ formation rate from the doublet μd state.
λ_{qd}	Hyperfine transition rate from the quartet to the doublet μd state.
λ_q	$dd\mu$ formation rate from the quartet μd state.
Λ_d	Muon capture rate from the doublet μd state.
Λ_{He}	Total muon capture rate on a ^{3}He.
Λ_q	Muon capture rate from the quartet μd state.
Λ_S	Muon capture rate from the singlet μp state.